The Astrophysical Journal Letters, 992:L18 (23pp), 2025 October 20 https://doi.org/10.3847/2041-8213/ae0a26

The First Radio-bright Off-nuclear Tidal Disruption Event AT 2024tvd Reveals the Fastest-evolving Double-peaked Radio Emission

Itai Sfaradi[1,2], Raffaella Margutti[1,2,3], Ryan Chornock[1,2], Kate D. Alexander[4], Brian D. Metzger[5,6], Paz Beniamini[7,8,9], Rodolfo Barniol Duran[10], Yuhan Yao[1,2,11], Assaf Horesh[12], Wael Farah[1,13,14], Edo Berger[15], Nayana A. J.[1,2], Yvette Cendes[16,17], Tarraneh Eftekhari[18], Rob Fender[19], Noah Franz[4], Dave A. Green[20], Erica Hammerstein[1,2], Wenbin Lu[1,2,21], Eli Wiston[1,2], Yirmi Bernstein[12], Joe Bright[19], Collin T. Christy[4], Luigi F. Cruz[13], David R. DeBoer[22,23], Walter W. Golay[15], Adelle J. Goodwin[24], Mark Gurwell[15], Garrett K. Keating[15], Tanmoy Laskar[25], James C. A. Miller-Jones[24], Alexander W. Pollak[13], Ramprasad Rao[15], Andrew Siemion[13,14,19,26,27,28], Sofia Z. Sheikh[13,14], Nadav Shoval[12], and Sjoert van Velzen[29]

[1] Department of Astronomy, University of California, Berkeley, CA 94720-3411, USA; itai.sfaradi@berkeley.edu
[2] Berkeley Center for Multi-messenger Research on Astrophysical Transients and Outreach (Multi-RAPTOR), University of California, Berkeley, CA 94720-3411, USA
[3] Department of Physics, University of California, 366 Physics North MC 7300, Berkeley, CA 94720, USA
[4] Department of Astronomy and Steward Observatory, University of Arizona, 933 North Cherry Avenue, Tucson, AZ 85721-0065, USA
[5] Department of Physics and Columbia Astrophysics Laboratory, Columbia University, New York, NY 10027, USA
[6] Center for Computational Astrophysics, Flatiron Institute, 162 5th Avenue, New York, NY 10010, USA
[7] Department of Natural Sciences, The Open University of Israel, P.O Box 808, Ra'anana 4353701, Israel
[8] Astrophysics Research Center of the Open University (ARCO), The Open University of Israel, P.O Box 808, Ra'anana 4353701, Israel
[9] Department of Physics, The George Washington University, 725 21st Street NW, Washington, DC 20052, USA
[10] Department of Physics and Astronomy, California State University, Sacramento, 6000 J Street, Sacramento, CA 95819-6041, USA
[11] Miller Institute for Basic Research in Science, 206B Stanley Hall, Berkeley, CA 94720, USA
[12] Racah Institute of Physics, The Hebrew University of Jerusalem, Jerusalem 91904, Israel
[13] SETI Institute, 339 Bernardo Avenue, Suite 200, Mountain View, CA 94043, USA
[14] Berkeley SETI Research Centre, University of California, Berkeley, CA 94720, USA
[15] Center for Astrophysics |Harvard & Smithsonian, 60 Garden Street, Cambridge, MA 02138-1516, USA
[16] Department of Physics, University of Oregon, 1371 E 13th Avenue, Eugene, OR 97403, USA
[17] Institute for Fundamental Science, University of Oregon, 1371 E 13th Avenue, Eugene, OR 97403, USA
[18] Center for Interdisciplinary Exploration and Research in Astronomy (CIERA), Northwestern University, 1800 Sherman Avenue, Evanston, IL 60201, USA
[19] Astrophysics, Department of Physics, University of Oxford, Keble Road, Oxford, OX1 3RH, UK
[20] Astrophysics Group, Cavendish Laboratory, J. J. Thomson Avenue, Cambridge CB3 0US, UK
[21] Theoretical Astrophysics Center, University of California, Berkeley, CA 94720-3411, USA
[22] Radio Astronomy Laboratory, University of California, Berkeley, CA 94720, USA
[23] Sub-department of Astrophysics, University of Oxford, Oxford, OX1-3RH, UK
[24] International Centre for Radio Astronomy Research–Curtin University, GPO Box U1987, Perth, WA 6845, Australia
[25] Department of Physics & Astronomy, University of Utah, Salt Lake City, UT 84112, USA
[26] Breakthrough Listen, Astrophysics, Department of Physics, The University of Oxford, Keble Road, Oxford OX1 3RH, UK
[27] Department of Physics and Astronomy, University of Manchester, UK
[28] University of Malta, Institute of Space Sciences and Astronomy, Msida, MSD2080, Malta
[29] Leiden Observatory, Leiden University, Postbus 9513, 2300 RA, Leiden, The Netherlands
Received 2025 August 5; revised 2025 September 15; accepted 2025 September 17; published 2025 October 13

Abstract

We present the first multiepoch broadband radio and millimeter monitoring of an off-nuclear tidal disruption event (TDE) using the Very Large Array, the Atacama Large Millimeter/submillimeter Array, the Allen Telescope Array, the Arcminute Microkelvin Imager Large Array, and the Submillimeter Array. The off-nuclear TDE AT 2024tvd exhibits double-peaked radio light curves and the fastest-evolving radio emission observed from a TDE to date. With respect to the optical discovery date, the first radio flare rises faster than $F_\nu \sim t^9$ at $\Delta t = 88$–131 days and then decays as fast as $F_\nu \sim t^{-6}$. The emergence of a second radio flare is observed at $\Delta t \approx 194$ days with an initial fast rise of $F_\nu \sim t^{18}$ and an optically thin decline of $F_\nu \sim t^{-12}$. We interpret these observations in the context of a self-absorbed and free–free absorbed synchrotron spectrum, while accounting for both synchrotron and inverse Compton cooling. We find that a single prompt outflow cannot easily explain these observations and that it is likely that either there is only one outflow that was launched at $\Delta t \sim 80$ days or there are two distinct outflows, with the second launched at $\Delta t \sim 170$–190 days. The nature of these outflows, whether sub-, mildly, or ultrarelativistic, is still unclear, and we explore these different scenarios. Finally, we find a temporal coincidence between the launch time of the first radio-emitting outflow and the onset of a power-law component in the X-ray spectrum, attributed to inverse Compton scattering of thermal photons.

Unified Astronomy Thesaurus concepts: Tidal disruption (1696); Supermassive black holes (1663); Radio astronomy (1338); Time domain astronomy (2109)

Materials only available in the online version of record: machine-readable table

1. Introduction

Tidal disruption events (TDEs) occur when a star is torn apart by the extreme tidal forces of a massive black hole (MBH; J. G. Hills 1975; M. J. Rees 1988). These cataclysmic events produce radiation across the electromagnetic spectrum, providing valuable information on the demographics of MBHs, the resulting accretion processes, the fast outflows generated during stellar disruption and disk formation, and the various physical mechanisms governing TDEs (K. D. Alexander et al. 2020; S. van Velzen et al. 2021; E. Hammerstein et al. 2023; Y. Yao et al. 2023; M. Guolo et al. 2024). Most TDEs are observed in galactic nuclei, with a small offset from the host nucleus serving as a classification criterion in many cases (E. Hammerstein et al. 2023). However, a distinct subset known as off-nuclear TDEs occurs outside the central regions of galaxies and can be associated with wandering (A. Ricarte et al. 2021a, 2021b) or recoiling (N. Stone & A. Loeb 2011) BHs, with only a handful of off-nuclear TDE candidates discovered so far (D. Lin et al. 2018, 2020; A. J. Goodwin et al. 2025a; I. Grotova et al. 2025; M. Guolo & A. Mummery 2025; C. C. Jin et al. 2025; Y. Yao et al. 2025b). Studying these events presents a unique opportunity to probe MBH populations beyond galactic nuclei, investigate the potential presence of intermediate-mass BHs (IMBHs), and explore the dynamics of MBHs before and after coalescence in nontraditional environments.

The interaction between the fast outflows from TDEs (e.g., unbound tidal debris stream, winds from the accretion disk, and relativistic jets) and the surrounding medium can generate shocks, producing nonthermal synchrotron emission (e.g., K. D. Alexander et al. 2020). Since this nonthermal emission typically peaks at radio wavelengths, radio observations play a key role in studying the interaction region. Early-time radio emission, detected within the first few weeks to months after optical discovery, has been observed in approximately 30% of optically detected TDEs (K. D. Alexander et al. 2020), revealing a wide range of outflow properties. For example, the kinetic energy associated with these outflows spans several orders of magnitude, from $\sim 10^{48}$–10^{50} erg for subrelativistic and mildly relativistic outflows (e.g., ASASSN-14li, K. D. Alexander et al. 2016; J. Krolik et al. 2016; AT 2019dsg, R. Stein et al. 2021; Y. Cendes et al. 2022) to $\sim 10^{51}$–10^{53} erg for relativistic jets (e.g., Swift J1644+57, B. A. Zauderer et al. 2011; E. Berger et al. 2012; T. Eftekhari et al. 2018; P. Beniamini et al. 2023; AT 2022cmc, I. Andreoni et al. 2022; L. Rhodes et al. 2023; the possible off-axis relativistic jet from AT 2018hyz, T. Matsumoto & T. Piran 2023; I. Sfaradi et al. 2024; Y. Cendes et al. 2025).

Subrelativistic outflows, with typical velocities of up to a few times $0.1c$, are typically associated with the unbound stellar debris stream, accretion-driven winds, or stream–stream collisions (e.g., ASASSN-14li, K. D. Alexander et al. 2016; the first flare from AT 2020vwl, A. J. Goodwin et al. 2023; potentially AT 2019dsg, Y. Cendes et al. 2022; see also R. Stein et al. 2021, for an alternative explanation). If these outflows originate from the unbound stellar debris or accretion disk winds, the resulting radio emission provides a rare opportunity to probe the circumnuclear medium (CNM) on scales of 10^{15}–10^{17} cm. Relativistic jets probe the CNM, or the interstellar medium (ISM), at much larger distances, typically 10^{17}–10^{19} cm. On the other hand, radio emission from stream–stream collisions can shed light on the density structure of the unbound tidal debris stream.

Approximately 40% of optically discovered TDEs exhibit late-time radio brightening months to years after stellar disruption (Y. Cendes et al. 2024; K. D. Alexander et al. 2025). Additionally, some TDEs show multiple flares in their radio light curves on different timescales (e.g., ASASSN-15oi, A. Horesh et al. 2021a; A. Hajela et al. 2025; AT 2019azh, I. Sfaradi et al. 2022; AT 2020vwl, A. J. Goodwin et al. 2023). Several mechanisms have been proposed to explain these late-time flares, and they are broadly divided into (a) those that invoke an outflow that is launched around the time of optical discovery and is either interacting with a complex density structure (A. Horesh et al. 2021b; T. Matsumoto & T. Piran 2024) or initially pointing away from our line of sight (T. Matsumoto & T. Piran 2023; C. T. Christy et al. 2024; I. Sfaradi et al. 2024; Y. Cendes et al. 2025), and (b) those that require a delayed launch of an outflow (potentially accretion-driven outflow; D. Giannios & B. D. Metzger 2011; A. Horesh et al. 2021a; Y. Cendes et al. 2022; I. Sfaradi et al. 2022; A. J. Goodwin et al. 2025b; A. L. Piro & B. Mockler 2025).

TDE-driven fast outflows also provide a natural laboratory for studying the microphysics of both nonrelativistic and relativistic shock waves. Electrons at the shock front are accelerated to relativistic velocities, typically forming a power-law energy distribution. Observations of the optically thin regime of the synchrotron spectrum offer a unique probe of this power-law index, which encodes information about the process of particle acceleration (e.g., D. Caprioli 2024). A fraction of the post-shock energy is divided between the electrons and the magnetic field, often assumed to be in equipartition for the lack of better observational guidance (R. A. Chevalier 1998; R. Barniol Duran et al. 2013). However, when measurements of the synchrotron cooling spectral break are available, deviations from equipartition are often observed (e.g., AT 2019dsg, Y. Cendes et al. 2021; AT 2018hyz, Y. Cendes et al. 2022; ASASSN-19bt, C. T. Christy et al. 2024).

So far, radio observations have been reported for only three off-nuclear IMBH TDEs and TDE candidates. The IMBH TDE EP240222a was not detected with a 5σ upper limit of $\nu L_\nu \lesssim 10^{37}\,\mathrm{erg\,s^{-1}}$ (C. C. Jin et al. 2025). The other two IMBH TDE candidates, HLX-1 and eRASSt J142140–295321, revealed low levels of radio luminosity of $\nu L_\nu \simeq 5 \times 10^{36}$ erg s^{-1} and $3 \times 10^{37}\,\mathrm{erg\,s^{-1}}$, respectively (N. A. Webb et al. 2012; A. J. Goodwin et al. 2025a). However, the classification of these two transients as IMBH TDEs remains uncertain. This Letter discusses AT 2024tvd, the first off-nuclear TDE selected from optical sky surveys, which is also the first bona fide off-nuclear TDE with bright radio emission.

AT 2024tvd was discovered in the Zwicky Transient Facility (ZTF; E. C. Bellm et al. 2019; M. J. Graham et al. 2019) g band at a magnitude of 19.68 on 2024 August 25 (J. Sollerman et al. 2024) with the 48-inch Samuel Oschin Schmidt telescope at Palomar Observatory (P48). It was then

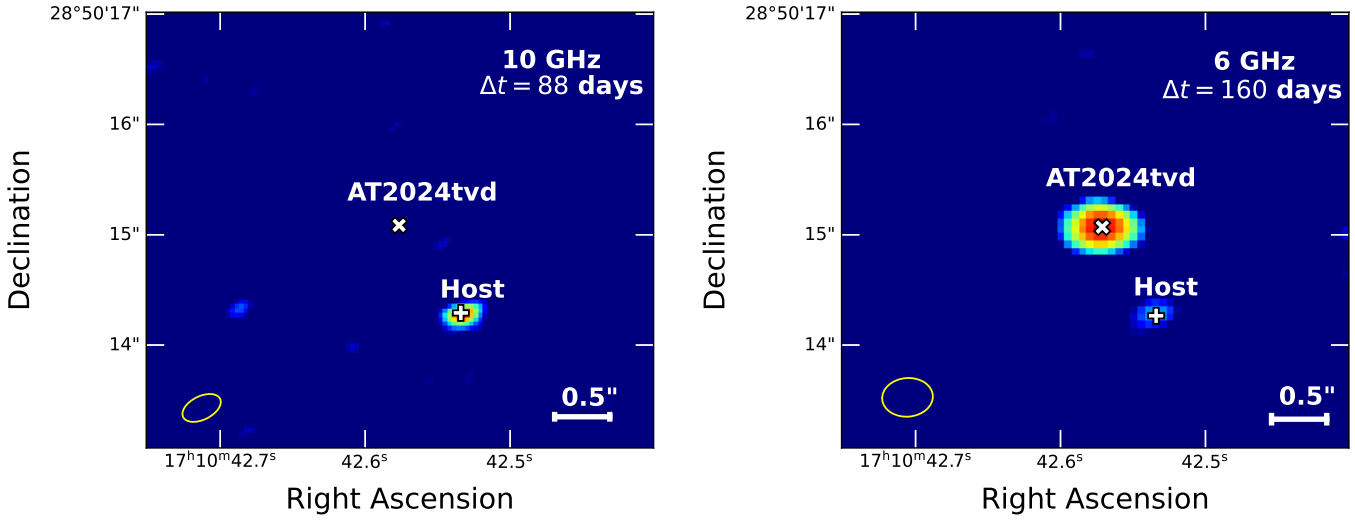

Figure 1. Radio images of the field of AT 2024tvd. Left panel: the first VLA observation in X band at $\Delta t = 88$ days, resulting in a null detection of the TDE and a detection of the nucleus of the host. Right panel: the VLA C-band image at $\Delta t = 160$ days, showing both the emission from the TDE and the emission from the host galaxy. The positions of the TDE and the nucleus obtained from the HST image (Y. Yao et al. 2025b) are marked with a cross and a plus sign, respectively. The size of the VLA clean beams is shown with a yellow ellipse in the lower left corner of each VLA image. The VLA images are scaled differently in order to show the full range of flux densities from the TDE and from the host galaxy nucleus.

classified as a TDE based on the broad H and He II in the spectrum, its central location in its host galaxy, and the long-lasting UV emission (S. Faris et al. 2024). The off-nuclear position of AT 2024tvd was first reported by Y. Yao et al. (2025a), and an MBH mass of 10^5–$10^7\,M_\odot$ at an offset of 0.8 kpc from the host nucleus was then estimated by Y. Yao et al. (2025b). The origin of the off-nuclear position of this TDE is likely to be a recoiling MBH from a triple MBH interaction or an MBH in the least massive galaxy of a minor galaxy merger. The reported redshift of AT 2024tvd is $z = 0.04494$, and we adopt a luminosity distance of 200 Mpc based on a standard ΛCDM cosmology with $\Omega_M = 0.3$, $\Omega_\Lambda = 0.7$, and a Hubble constant $H_0 = 70\,\mathrm{km\,s^{-1}\,Mpc^{-1}}$. All times and dates are given in UT.

In this Letter, we present comprehensive radio monitoring of AT 2024tvd (Section 2), and we find it to be the first radio-bright off-nuclear TDE and the TDE with the fastest evolution of the radio emission observed to date (Section 3). We model the radio emission from AT 2024tvd in the context of a self-absorbed synchrotron model, and we account (for the first time for a TDE in the radio) for both free–free absorption (FFA) by the material in front of the radio-emitting shock and inverse Compton (IC) cooling by the thermal optical/UV photons (see Section 4). We discuss the astrophysical implications of our analysis in Section 5, and we present our conclusions in Section 6.

2. Radio Observations

Following the optical classification of AT 2024tvd as a TDE (S. Faris et al. 2024), and the analysis of its off-nuclear position (first reported by Y. Yao et al. 2025a; see also Section 3), we triggered the Karl G. Jansky Very Large Array (VLA) on 2024 November 21, which corresponds to $\Delta t = 88$ days (Δt is the time since optical discovery in the frame of the observer), under our approved program to follow up TDEs (VLA 24A-386; PI: Alexander). This X-band observation ($\nu = 10$ GHz) resulted in a nondetection at the coordinates of the TDE. Instead, a point-source emission at the coordinates of the host's nucleus was detected (see left panel of Figure 1). Broadband follow-up observations in S–Ku bands (centered around 3–15 GHz) of the field of AT 2024tvd, conducted on 2025 January 3, corresponding to $\Delta t = 131$ days, showed a point source at the position of the TDE and a point source at the position of the host galaxy nucleus in 3, 6, and 10 GHz (we first reported the 10 GHz detection from this observation in I. Sfaradi et al. 2025 and present a 6 GHz image in the right panel of Figure 1). Following this detection, we initiated a broadband, multiepoch campaign, using the VLA, the Atacama Large Millimeter/submillimeter Array (ALMA), the Arcminute Microkelvin Imager Large Array (AMI-LA; J. T. L. Zwart et al. 2008; J. Hickish et al. 2018), the Allen Telescope Array (ATA; W. Farah et al. 2025, in preparation, A. W. Pollak et al. 2025, in preparation), and the Submillimeter Array (SMA). We emphasize here that our analysis takes into account the underlying emission from the host galaxy nucleus for observations that do not resolve the transient and the host (see detailed discussions in Sections 2.1 and 2.4 and Appendix B).

2.1. Karl G. Jansky Very Large Array

We observed the field of AT 2024tvd with the VLA under our dedicated TDE program (VLA 24A-386; PI: Alexander) and a Director's Discretionary Time (DDT) program (VLA 25A-483; PI. Sfaradi). In all of our observations we used J1735+3616 as a phase calibrator. 3C 147 and 3C 48 were used as bandpass and absolute flux calibrators. Our first four observations were conducted while the VLA was in its most extended A configuration. The fifth observation with the VLA was conducted with the transitional A→D configuration. All of the following observations were made while the VLA was in the more compact C and D configurations. We used the Common Astronomy Software Applications (CASA; CASA Team et al. 2022) packages and the VLA calibration pipeline to flag and calibrate the data. Additional manual flagging was applied when needed.

We used the CASA task `TCLEAN` to produce clean images of the field of AT 2024tvd. Our S- and C-band images taken in A configuration showed both the emission from the host

Table 1
Summary of the Radio Flux Measurements

Observation Date (DD-MM-YYYY)	Δt (days)	ν (GHz)	F_ν (mJy)	Image rms (mJy)	Telescope
21-11-2024	88	10	$\leqslant$0.0165	0.0055	VLA:A
03-01-2025	131	3	0.06 $\pm$ 0.02	0.013	VLA:A
03-01-2025	131	6	0.27 $\pm$ 0.03	0.008	VLA:A
03-01-2025	131	10	0.60 $\pm$ 0.06	0.011	VLA:A
03-01-2025	131	13	0.90 $\pm$ 0.10	0.018	VLA:A
03-01-2025	131	15	1.01 $\pm$ 0.10	0.015	VLA:A
03-01-2025	131	17	1.10 $\pm$ 0.11	0.014	VLA:A
11-01-2025	139	97.5	0.22 $\pm$ 0.03	0.027	ALMA

Note.
Summary of the radio flux density measurements for the off-nuclear TDE AT 2024tvd. Δt is the time since optical discovery (in the observer frame), ν is the observed central frequency, and F_ν is the flux density (and 1σ uncertainty); the image rms is also reported. In the "Telescope" column we specify different VLA configurations. Note that when analyzing VLA observations obtained in C and D configuration we removed a power-law fit to the observed host nucleus emission (see Appendix B). In addition, we cross-calibrated the ATA fluxes at $\Delta t = 249$ days with the VLA and removed the excess emission from the ATA observations owing to the contamination from the larger beam of the ATA. A full version of this table is accessible online in a machine-readable table format.

(This table is available in its entirety in machine-readable form in the online article.)

nucleus and the TDE (see Figure 1). When producing images while the VLA was in A configuration, we measure the flux density of both the transient and the host, if present, by using the CASA task `IMFIT` and the task `IMSTAT` to calculate the image rms. We then estimate the error of the flux density to be a quadratic sum of the error produced by the CASA task `IMFIT` and a 10% calibration error (K. W. Weiler et al. 1986). For observations taken in the VLA C or D configuration we measure only the flux density from the point source coincident with the TDE. Since we have measurements of the flux density from the nucleus, and since the flux density measured from these compact configuration images is contaminated by the host emission, when modeling the emission from the TDE we subtracted a power-law fit to the host nucleus emission as discussed in Appendix B.

Our observation from 2025 February 14, at $\Delta t = 173$ days, was conducted in a hybrid array, A $\rightarrow$ D. We then used only the long baselines by setting the `TCLEAN` parameter `uvrange` $> 15\,k\lambda$ to minimize the level of host contamination. While this procedure results in an elongated beam, it allows us to separate the host emission from the TDE emission. For this observation, we measure the flux density as the flux at the position of the optical transient (and not fitting a point source with `IMFIT`) and estimate the uncertainty to be a quadratic sum of the image rms calculated by the CASA task `IMSTAT` and a more conservative 15% calibration error (to account for possible systematic errors when using only long baselines).

We provide the flux density measurements in Table 1 and different images of the field of AT 2024tvd in Figure 1.

2.2. Atacama Large Millimeter/Submillimeter Array

Following our first detection with the VLA we obtained millimeter-band observations with ALMA in four epochs under two DDT programs (2024.A.00024.T and 2024.A.00034.T; PI. Sfaradi). We used ALMA Bands 3 and 5 with the central frequencies of 97.5 and 203 GHz, respectively, J1550+0527 as an absolute flux and bandpass calibrator, and J1753+2848 as a phase calibrator. We used the standard National Radio Astronomy Observatory (NRAO) calibrated images, fitted the point source with CASA task `IMFIT`, and used CASA task `IMSTAT` to obtain the image rms. We provide the flux density measurements in Table 1.

2.3. Arcminute Microkelvin Imager Large Array

AMI-LA is a radio interferometer that consists of eight antennas, each 12.8 m in diameter, with a maximum separation of 110 m. It observes with a 5 GHz bandwidth around a central frequency of 15.5 GHz. We observed the field of AT 2024tvd with AMI-LA with high cadence starting 2025 January 12, at $\Delta t = 140$ days, and reported the first detection in A. Horesh et al. (2025). We reduced, flagged, and calibrated our observations using `reduce_dc`, a customized AMI-LA data reduction software package (Y. C. Perrott et al. 2013). Images of the field of AT 2024tvd were produced using CASA task `TCLEAN` in an interactive mode. We fit the source at the optical position of the TDE with the CASA task `IMFIT` and calculated the image rms with the CASA task `IMSTAT`. We estimate the error of the peak flux density to be a quadratic sum of the error produced by the CASA task `IMFIT` and a 10% calibration error. We provide the flux density measurements in Table 1.

2.4. Allen Telescope Array

We observed the field of AT 2024tvd with the ATA under our program (P062; PI. Sfaradi) starting on 2025 March 20, which corresponds to $\Delta t = 207$ days. The ATA is a radio interferometer that comprises 42 dishes, each with a diameter of 6.1 m, and can utilize up to four independent frequency tunings in the range of 1–10 GHz, each with a width of $\sim$700 MHz (J. S. Bright et al. 2023). Our observations were centered around 1.5, 3, 5, and 8 GHz using 3C 286 to calibrate the absolute flux scale and bandpass response and 1735+362 to calibrate the time-dependent complex gains. We used a customized pipeline (https://github.com/joesbright/ATARI/) utilizing CASA to reduce the observations and CASA task `TCLEAN` for imaging.

The flux density measured by the ATA is contaminated by the background owing to the large beam of the ATA. Therefore, we cross-calibrated all the flux density measurements obtained with the ATA by removing the excess emission seen in the ATA observation on 2025 May 1 (at

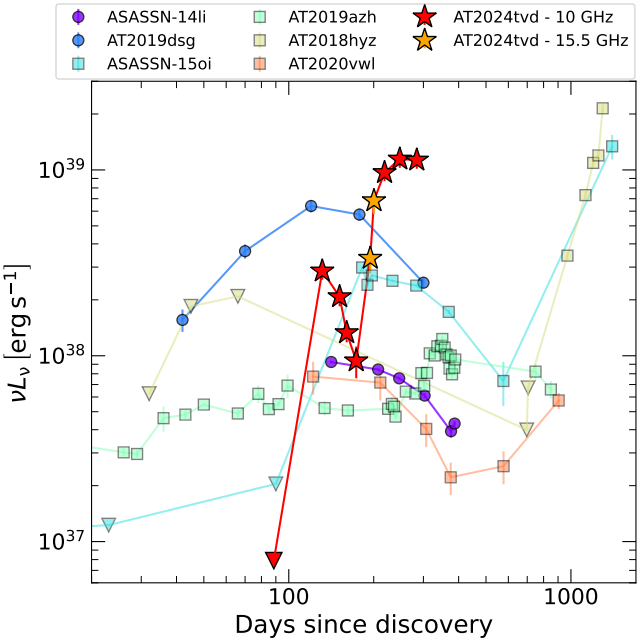

Figure 2. Radio luminosity evolution of a selection of known TDEs (ASASSN-14li, K. D. Alexander et al. 2016; ASASSN-15oi, A. Horesh et al. 2021a; AT 2019dsg, R. Stein et al. 2021; AT 2018hyz, Y. Cendes et al. 2022; AT 2019azh, A. J. Goodwin et al. 2022; I. Sfaradi et al. 2022; AT 2020vwl, A. J. Goodwin et al. 2023) and AT 2024tvd (this work; 10 GHz marked with red stars; 15.5 GHz marked with orange stars). Observations of the same TDE are connected with lines, and 3σ upper limits are plotted with triangles. The radio emission from the off-nuclear TDE AT 2024tvd reveals an extremely fast evolution compared to other TDEs, with a fast rise between $\Delta t = 88$ and 131 days, followed by a fast decline up to $\Delta t = 173$ days. Then, at $\Delta t = 194$ days, and about ~20 days since the last observation of the first radio flare, a second fast-rising radio flare emerges.

$\Delta t = 249$ days), compared to the flux density measured by the VLA on 2025 April 29 (at $\Delta t = 247$ days). We estimate the error of the peak flux density to be a quadratic sum of the error produced by CASA task `IMFIT` and a 15% calibration error. We provide the flux density measurements in Table 1.

2.5. Submillimeter Array

Beginning 2025 April 21 ($\Delta t = 239$ days), several observations of AT 2024tvd were conducted with the SMA, as part of the Pursuit of Extragalactic Transients with the SMA (POETS) Large-Scale SMA program (2022B-S046; PI: E. Berger). SMA observations were conducted with the array in compact configuration ($\theta_b = 3\farcs5 \times 3\farcs2$), tuned to a local oscillator frequency of 225.5 GHz, providing spectral coverage in the ranges of 209.5–221.5 GHz and 229.5–241.5 GHz. For all observations, 3C 279 was observed as a bandpass calibrator, Vesta was observed as the flux calibrator, and 1642+398 and 1658+347 were observed as gain calibrators, with a 12-minute cycle time cadence.

Analysis of the data was performed using the SMA COMPASS pipeline (G. K. Keating et al. 2025, in preparation), which derives bandpass and gains calibration tables, and flags outlier visibilities and baselines where limited or no coherence is seen on calibration targets. Flux calibration uses the Butler-JPL-Horizons 2012 (B. Butler 2012) model for Vesta. The data were imaged, and deconvolution was performed via the CLEAN algorithm (J. A. Högbom 1974). We provide the flux density measurements in Table 1.

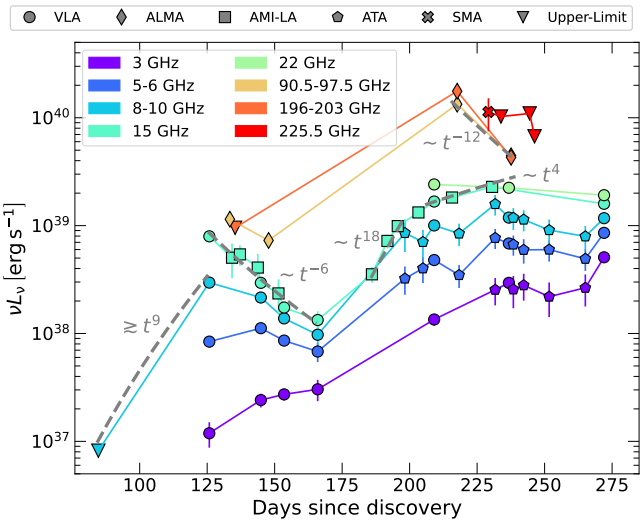

Figure 3. Radio light curves of the off-nuclear TDE AT 2024tvd at different frequencies. We plot temporal power laws for different segments of these light curves (with the reference initial time being the optical discovery), showing the fast rise and decay in both flares.

3. Radio Emission from AT 2024tvd: Broad Considerations

Next, we present the entire set of radio observations we have obtained at $\Delta t \leqslant 284$ days. We begin by examining the overall evolution of the radio emission from AT 2024tvd over ~200 days, with observations spanning from the centimeter to the millimeter bands. We discuss the emission from the host galaxy nucleus in Appendix B. In Figure 2 we plot the 10 GHz light curve of AT 2024tvd compared to other known radio-bright TDEs. Figure 3 presents light curves in different centimeter and millimeter bands together with temporal power-law indices with respect to the optical discovery date. In Figure 4 we present the different spectral energy distributions (SEDs) with the best-fitting broken power-law functions (see detailed discussion in Section 4.1). Overall, as seen from these plots, this TDE exhibits two episodes of fast-evolving radio emission, with distinct broadband evolution in each flare.

Our 10 GHz observation at $\Delta t = 88$ days did not reveal any detectable emission from the TDE with a luminosity upper limit of $\nu L_\nu < 7.9 \times 10^{36}$ erg s^{-1}. At $\Delta t = 131$ days the 10 GHz flux density is $\geqslant$40 times larger than the initial upper limit, and the broadband SED indicates an optically thick emission, with a possible transition to the radio spectral peak around 17 GHz at an observed peak luminosity of $\nu L_\nu \approx 9 \times 10^{38}$ erg s^{-1}. The following broadband SEDs, up to $\Delta t = 173$ days, exhibit a fast decline of the peak flux density and of the peak frequency (see left panel of Figure 4). In addition, the spectral shape of the SED evolved as well. The first ALMA observation, at $\Delta t = 139$–141 days, showed an optically thin spectral slope higher than $F_\nu \sim \nu^{-1.2}$ (based on the detection at 97.5 GHz and the upper limit at 203 GHz). A later VLA+ALMA SED, obtained at $\Delta t = 151$–154 days, revealed an optically thin emission of $F_\nu \sim \nu^{-0.55}$. These spectral slopes, together with the SED obtained at $\Delta t = 131$ days, imply the presence of an evolving spectral break frequency in the SED. This break frequency, typically associated with the cooling frequency ν_c (in which the synchrotron-emitting electrons quickly lose energy to radiation; see detailed discussion in Section 4), evolved from 17 GHz $< \nu_c <$ 97.5 GHz to $\nu_c \geqslant$ 97.5 GHz between these two epochs.

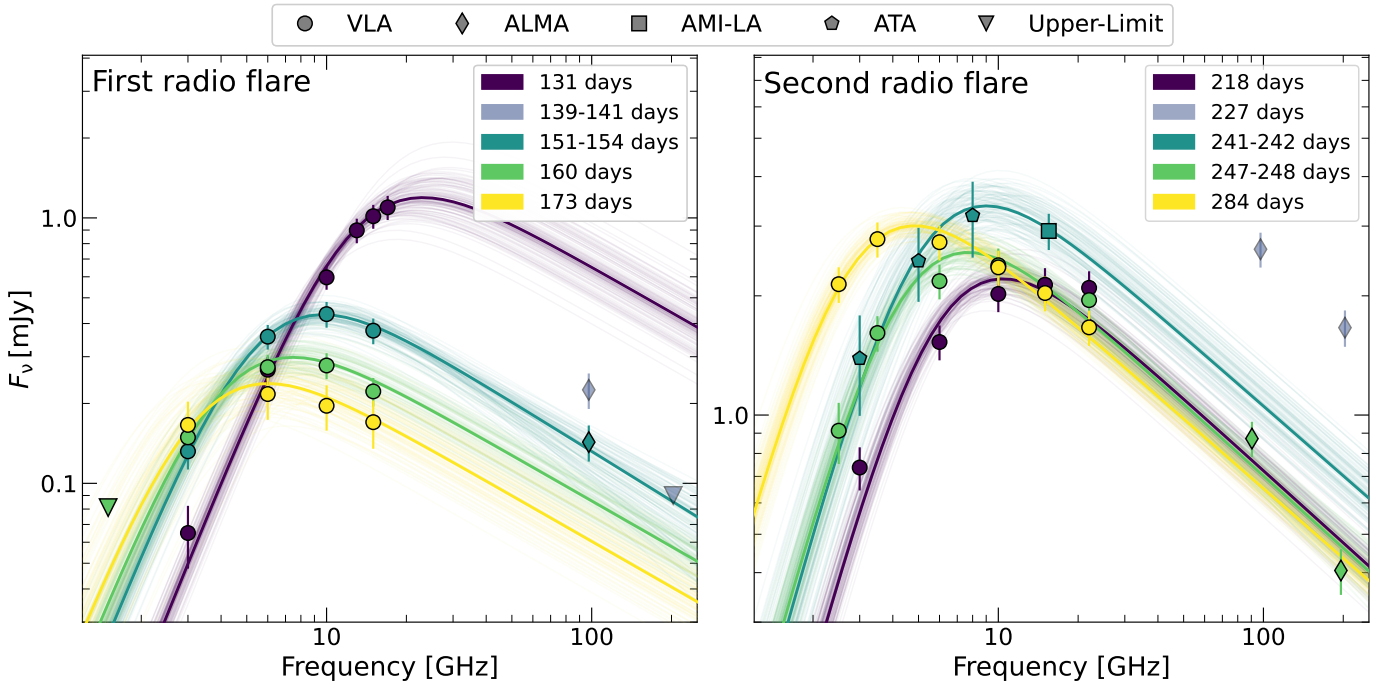

Figure 4. Broadband radio SEDs of the off-nuclear TDE AT 2024tvd. The left panel shows the radio SEDs of the first radio flare, and the right panel is for the second radio flare. Detections obtained with different radio telescopes are marked with different markers (circles for the VLA, diamonds for ALMA, squares for AMI-LA, and pentagons for the ATA), and triangles mark 3σ upper limits. We fitted these SEDs with the broken power-law function described in Equation (4) (see detailed discussion in Section 4.1).

At $\Delta t = 194$ days, a rebrightening of the radio emission was observed with AMI-LA at 15.5 GHz. The evolution of this second radio flare is extremely peculiar. The observed peak luminosity is a factor of $\sim$3 higher than the observed peak luminosity of the first radio flare. Furthermore, the temporal evolution of the broadband SEDs does not follow the temporal evolution of the first radio flare. The optically thin emission, seen in the millimeter bands, showed a fast decline, and the spectral peak flux, on the other hand, rises while its peak frequency slowly moves to the lower-GHz bands.

In the first flare, assuming for now the optical discovery date as the reference time, the rise from the first upper limit ($\Delta t = 88$ days) to the first radio detection ($\Delta t = 131$ days) is at least as fast as $F_\nu \sim t^9$. Then, the radio spectral peak declines as $F_p \sim t^{-6}$, and the peak frequency also declines quickly, $\nu_p \sim t^{-5}$. For the second flare, the detailed 15.5 GHz light curve we obtained (see Figure 3) exhibits an extremely fast evolution of $F_{15.5\,\mathrm{GHz}} \sim t^{18}$, which then changes to $F_{15.5\,\mathrm{GHz}} \sim t^4$. Furthermore, the optically thin emission of the second flare, observed in the millimeter bands, revealed an unprecedented fast decline of $F_\nu \sim t^{-12}$ (see Figure 3).

About 40% of the optically discovered TDEs show a late-time brightening of the radio emission (Y. Cendes et al. 2024). Naturally, as these TDEs rise at late times, a fast evolution of their radio emission with reference to their optical discovery date is expected. More specifically, when fitting the rise or the decay of the radio light curve with a temporal power law, $F_\nu \sim t^\alpha$, a power-law index of $|\alpha| > 3$ is achieved. For example, the radio spectral peak of AT 2018hyz evolved as $F_p \simeq t^5$ (Y. Cendes et al. 2022). However, even compared to other radio-bright TDEs, the temporal evolution of the radio emission observed for AT 2024tvd is the fastest ever seen in TDEs (see Figure 2).

The late-time emergence of the radio emission (for each flare separately) can mean that (a) a prompt subrelativistic outflow was launched around the time of optical discovery, interacting with a complex medium; (b) a delayed subrelativistic outflow was launched at $\Delta t > 0$ days; (c) a relativistic jet was launched around the time of optical discovery and the emission from this jet is entering our line of sight at late times; or (d) a relativistic jet was launched at late times and we observed it either on- or off-axis. In Section 4, we consider these different scenarios for the origin of the radio-emitting outflow(s). We discuss the astrophysical implications of our findings in Section 5.

4. Detailed Modeling of the Radio Emission

Radio emission from transients is typically associated with synchrotron radiation generated in shocks as a result of fast-moving outflows. In the following subsections, we explore the possibilities of a prompt outflow (launched around the time of optical discovery), delayed outflows, and off-axis relativistic jets. In the standard picture of synchrotron radiation, at the shock front, electrons are accelerated to relativistic velocities and gain a power-law distribution of Lorentz factors, $N(\gamma)\, d\gamma \propto \gamma^{-p}\, d\gamma$; $\gamma \geqslant \gamma_m$, where γ_m is the Lorentz factor of the lowest-energy electrons, and magnetic fields are compressed and generated owing to the runaway Weibel instability (E. S. Weibel 1959; R. A. Chevalier 1998; R. Sari et al. 1998). The presence of synchrotron self-absorption (SSA) results in a broken power-law synchrotron spectrum, where the exact spectral shape depends on the order of the minimal frequency ν_m (which corresponds to γ_m), the SSA frequency ν_{sa}, and the cooling frequency ν_c (which corresponds to γ_c), above which electrons are losing significant energy to radiation (see J. Granot & R. Sari 2002 for the exact spectral shapes).

So far, the radio TDE literature has focused on synchrotron cooling as the dominant cooling mechanism. However, another important electron cooling mechanism is (external) IC cooling in which thermal optical/UV photons are scattered to the X-ray band by the relativistic electrons at the shock front. This is most commonly used in the analysis of supernovae (R. A. Chevalier & C. Fransson 2006; R. Margutti et al. 2012; A. J. Nayana et al. 2025), and we consider it here for the first time in the context of TDEs (see detailed discussions in Section 4.2 and Appendix A). In the slow-cooling regime, where $\nu_m < \nu_c$, and in the regime where $\nu_m < \nu_{\rm sa}$, the radio spectral peak is at $\nu_{\rm sa}$, and a power-law index of $F_\nu \sim \nu^{5/2}$ is expected for the optically thick regime above ν_m. If $\nu_m > \nu_{\rm sa}$, the optically thick regime is expected to have a shallower slope of $F_\nu \sim \nu^2$. In the optically thin regime, and for $\nu_{\rm sa} < \nu_c$, the flux density is $F_\nu \sim \nu^{-(p-1)/2}$ for $\nu < \nu_c$ and $F_\nu \sim \nu^{-p/2}$ for $\nu > \nu_c$. For $\nu_{\rm sa} > \nu_c$ the optically thin regime is dominated by a single power law, $F_\nu \sim \nu^{-p/2}$. Finally, in cases where the material in front of the synchrotron-generating shock is dense, external FFA can dominate in radio wavelengths and suppress the synchrotron emission. This external FFA was not considered so far for radio-emitting TDEs, and we apply it for the first time in our analysis in Section 4.2.

A common assumption is that a fraction, ϵ_e, of the post-shock energy density, $u_{\rm ps} = \frac{9}{8}\rho v_{\rm sh}^2$ (where ρ is the density of the surrounding ambient medium and $v_{\rm sh}$ is the velocity of the shock), is deposited in the relativistic electrons. A different fraction, ϵ_B, is deposited in the energy density of the magnetic fields, $u_B = B^2/8\pi$. The assumption of equipartition implies that $\epsilon_e = \epsilon_B$. Here the prefactor of $9/8$ in the post-shock energy assumes it to be the thermal energy of a strong shock with an adiabatic index of $\gamma = 5/3$, but we note that an order-of-unity correction to this energy is introduced for different scenarios (see the discussion in the Appendix of L. DeMarchi et al. 2022).

In Section 4.1, we analyze individual broadband SEDs in the context of an SSA model for different physical scenarios. While this form of analysis is very useful when inferring the physical parameters of the shock and its environment, it does not take into account the dynamics of the outflow. Therefore, with the purpose of also accounting for the shock dynamics, in Section 4.2 we apply a time-dependent model to the radio observations of the first flare in the context of a nonrelativistic outflow that interacts with a simple density profile.

4.1. Analysis and Modeling of Individual SEDs

For a self-absorbed synchrotron spectrum, the radius of the radio-emitting region and the magnetic field strength can be inferred from the spectral peak of the radio emission. Here we use the Newtonian formalism introduced in R. A. Chevalier (1998) since the inferred velocities in the spherical outflow scenario are subrelativistic (see following subsections); however, we note that in the case of a relativistic outflow the formalism introduced in R. Barniol Duran et al. (2013) is more suitable. If the spectral peak is dominated by $\nu_{\rm sa}$ and $\nu_{\rm sa} < \nu_c$, R. A. Chevalier (1998) showed that the radius is given by

$$R = \left[\frac{6c_6^{p+5}F_{\nu_{\rm sa}}^{p+6}d_{\rm l}^{2p+12}}{\alpha f(p-2)\pi^{p+5}c_5^{p+6}E_{\rm l}^{p-2}}\right]^{1/(2p+13)}\left(\frac{\nu_{\rm sa}}{2c_1}\right)^{-1} \quad (1)$$

and the magnetic field strength is

$$B = \left[\frac{36\pi^3 c_5}{\alpha^2 f^2 (p-2)^2 c_6^3 E_l^{2(p-2)} F_{\nu_{\rm sa}} d_{\rm l}^2}\right]^{2/(2p+13)}\left(\frac{\nu_{\rm sa}}{2c_1}\right), \quad (2)$$

where $F_{\nu_{\rm sa}}$ is the peak flux density at the intersection between the optically thick and thin regimes of the synchrotron self-absorbed SED; $d_{\rm l}$ is the distance to the TDE; f is the emission volume filling factor; $\alpha \equiv \epsilon_{\rm e}/\epsilon_{\rm B}$; c_1, c_5, and c_6 are constants provided in A. G. Pacholczyk (1970); and E_l is the electron's rest-mass energy. Under the assumption of a strong shock, the number density of the surrounding, preshock, ambient medium is given by

$$n_e = \frac{1}{9\pi\mu_e m_p}\epsilon_B^{-1}B^2 v_{\rm sh}^{-2}, \quad (3)$$

where m_p is the mass of a proton and μ_e is the mean molecular weight per electron (throughout our analysis we assume a fully ionized hydrogen composition, i.e., $\mu_e = 1$).

To obtain the peak flux density and its frequency, we adopt here a broken power-law function (see Equation (1) in J. Granot & R. Sari 2002)

$$F_\nu = F_p\left[\left(\frac{\nu}{\nu_p}\right)^{-s\beta_1} + \left(\frac{\nu}{\nu_p}\right)^{-s\beta_2}\right]^{-1/s}, \quad (4)$$

where F_p is the flux density at the intersection between the optically thick and thin regime at ν_p. In the $\nu_{\rm sa} < \nu_c$ scenario, $\beta_1 = 5/2$ and $\beta_2 = -(p-1)/2$. We fix[30] the smoothing parameter, s, to $1.25p$–$0.18p$.

We use `emcee` (D. Foreman-Mackey et al. 2013) to determine the best-fit parameters and infer their posterior distributions using flat priors. We use 200 walkers with 5000 steps for each chain and discard the first 100 steps for burn-in. For both the first and second radio flares, the broadband SEDs obtained with the VLA, ATA, and AMI-LA do not probe the transition from the spectral peak to the optically thin regime to its full extent. Therefore, when fitting for the power-law index of the electrons, p, we combine VLA and ALMA observations separated by 2–3 days. For the first flare, we infer p based on VLA+ALMA observations at $\Delta t = 151$–154 days and apply it to observations at $\Delta t = 131$, 160, and 173 days. For the second flare, we infer p based on VLA+ALMA observations at $\Delta t = 247$–248 days and apply it to observations at $\Delta t = 218$ days, 241–242 days, and 284 days. We note that while our fitting process constrains F_p and ν_p at $\Delta t = 131$ days, this SED shows mostly optically thick emission, with only a slight transition to the radio spectral peak at the high frequencies in 13–17 GHz. In addition, for the SED fitted at $\Delta t = 241$–242 days we used only ATA and AMI-LA data, and the ATA observations suffer from contamination because of its large beam. Therefore, we treat the inferred values from these epochs with caution. The results of these fits are reported in Table 2, and we plot the best-fitting models in Figure 4.

Based on the analysis above, we infer $F_p \sim t^{-6}$ and $\nu_p \sim t^{-5}$ during the first flare and $F_p \sim t^{1.2}$ and $\nu_p \sim t^{-3}$ during the late phases of evolution of the second flare. We next use these best-

[30] We note here that this value is given by J. Granot & R. Sari (2002) for a wind-like density profile, i.e., $\rho \propto r^{-2}$. We later find that a steeper density profile is more suitable. However, the choice of the smoothing parameter does not change our conclusions.

Table 2
Broken Power-law Fits to Individual SEDs

Δt (days)	F_p (mJy)	ν_p (GHz)	p
131	$2.08^{+0.28}_{-0.23}$	$13.2^{+1.3}_{-1.1}$	2.14[a]
151–154	$0.78^{+0.09}_{-0.07}$	$5.71^{+0.52}_{-0.44}$	$2.14^{+0.21}_{-0.14}$
160	$0.52^{+0.05}_{-0.04}$	$4.28^{+0.38}_{-0.35}$	2.14[a]
173	0.41 ± 0.05	$3.43^{+0.59}_{-0.53}$	2.14[a]
218	3.87 ± 0.25	$6.03^{+0.47}_{-0.43}$	2.17[a]
241–242	5.86 ± 0.49	$5.12^{+0.67}_{-0.58}$	2.17[a]
247–248	$4.46^{+0.40}_{-0.36}$	$4.40^{+0.37}_{-0.30}$	2.17 ± 0.10
284	5.29 ± 0.22	2.80 ± 0.20	2.17[a]

Notes. Best-fitting parameters of the radio SEDs using Equation (4). The reported times and peak frequencies are in the frame of the observer.
[a] Marks observations for which the power-law index of the electron distribution is fixed (see discussion in Section 4.1).

fitting parameters to derive the physical parameters of the shock. In the following subsections we explore different outflow scenarios using the results from the individual fits. In Section 4.2 we do a time-dependent analysis in the context of a subrelativistic outflow for the first radio component only.

4.1.1. A Prompt, Nonrelativistic Outflow

First, we assume (1) that the outflow was launched around the time of optical discovery, (2) equipartition ($\epsilon_e = \epsilon_B = 0.1$), and (3) an emission filling factor $f = 0.5$, to derive (i) the equipartition radius (Equation (1)), (ii) the magnetic field strength (Equation (2)), (iii) the density profile of the surrounding medium (Equation (3)), and (iv) the energy of the event by assuming that the energy in the magnetic fields is a fraction of the post-shock energy

$$U_{\rm ps} = \epsilon_{\rm B}^{-1}\frac{B^2}{8\pi}V, \tag{5}$$

where $V = \frac{4\pi}{3} f R^3$ is the volume of the emitting region. In Figure 5 we present the results of this analysis, and we provide the inferred physical parameters in Table 3.

We find that the inferred velocities are subrelativistic for both flares (see Figure 5). Interestingly, the radius derived from the first SED of the second radio flare matches the radius evolution during the first radio flare. This suggests that both radio flares are a result of the same outflow. However, we cannot estimate the radius of the emitting region during the second radio flare before the first broadband SED. Therefore, the fact that the initial radius estimation during the second radio flare matches the observed evolution during the first radio flare might also be a coincidence. These results also imply significant acceleration, $R \sim t^{2.5}$ and $R \sim t^{3.5}$ for the first and second radio components, respectively. The initial equipartition energy of the first flare is $\sim 4 \times 10^{48}$ erg at $\Delta t = 131$ days and then declines with time. The energy of the second flare increases with time, reaching $\sim 6 \times 10^{49}$ erg at $\Delta t = 284$ days, a factor of $\simeq 10$ higher than the first flare (see Figure 5). This overall behavior motivates the scenarios of two distinct delayed outflows and/or off-axis relativistic jets.

The inferred density of the surrounding medium depends on the velocity of the shock (Equation (3)). Here we estimate the velocity for each epoch by $v_{\rm sh} = R/\Delta t$ since we are conducting a time-independent analysis (see Section 4.2 for a time-dependent analysis). For the first flare, we find $n_e = (4.0^{+1.6}_{-0.9}) \times 10^4\,{\rm cm}^{-3}$ at $R = (2.10^{+0.15}_{-0.12}) \times 10^{16}$ cm and a very steep density profile, $n_e \sim r^{-5}$ (see bottom panel of Figure 5). However, extrapolating this density profile to the time of the first radio nondetection ($\Delta t = 88$ days) and assuming a similar velocity to the velocity measured at $\Delta t = 131$ days results in a 10 GHz flux density higher than the radio upper limit that was obtained at this time, even when accounting for external FFA by the dense medium in front of the radio-emitting shock.

Therefore, this density profile cannot explain the entire radio emission up to $\Delta t = 173$ days. One possibility is that there is a change in the density profile at $R < 2 \times 10^{16}$ cm. In the case of a density cavity, the emission at $\Delta t = 88$ days is too faint to be detected. On the other hand, if there is an overdensity at these small radii, the radio emission can be suppressed by FFA by the dense medium in front of the shock. We discuss the densities needed to suppress the emission by FFA in Section 4.2 and Appendix A. Finally, the same analysis for the second radio flare (assuming a prompt outflow) requires a change in the density profile around $(4 - 6) \times 10^{16}$ cm and additional acceleration.

4.1.2. Delayed, Nonrelativistic Outflows

From the analysis above, the shock velocity is neither constant nor decelerating for $t_{\rm launch} = 0$ days, where we define $t_{\rm launch}$ as the launch time (in days from optical discovery) of the radio-emitting outflow. While one possibility for this observed behavior is shock acceleration, e.g., due to the propagation of the shock in a steep density profile of $\rho \sim r^{-s}$, with $s > 3$ density profile (E. Waxman & D. Shvarts 1993), it is also possible that one or two outflows were launched at $t_{\rm launch} > 0$ days, resulting in an apparent shock acceleration. To estimate the outflow launch time, we fit the equipartition radius with a function of the form $R(\Delta t) = \tilde{R}\left(\frac{\Delta t - t_{\rm launch}}{\Delta t_0 - t_{\rm launch}}\right)$, which assumes a constant outflow expansion velocity of $v_{\rm sh} \equiv \frac{\tilde{R}}{\Delta t_0 - t_{\rm launch}}$. We set $\Delta t_0 \equiv 131$ and 247 days for the first and second flares, respectively. $\tilde{R}$ and $t_{\rm launch}$ are free parameters. `emcee` is used to estimate the posteriors of the best-fitting parameters. For the first flare the outflow launching time is $t_{\rm launch} = 84^{+6}_{-25}$ days and the radius at $\Delta t_0 = 131$ days is $\tilde{R} = (2.1 \pm 0.1) \times 10^{16}$ cm; for the second flare $t_{\rm launch} = 170 \pm 10$ days and $\tilde{R} = (1.0 \pm 0.1) \times 10^{17}$ cm.

The equipartition radius and magnetic field strength do not depend on $t_{\rm launch}$. However, since $n_e \propto B^2 v_{\rm sh}^{-2}$ (Equation (3)) and we infer higher velocities, the assumption of a delayed outflow results in lower number density than in the case of $t_{\rm launch} = 0$ days. While the required densities are lower, the need for a steep $n_e(r)$ profile stays ($n_e \sim r^{-4}$ here vs. $n_e \sim r^{-5}$ in the prompt outflow scenario). In addition, if the first and second flares are manifestations of the same outflow (i.e., they share the same $t_{\rm launch}$), a density enhancement is still needed, and a shallower ($n_e \sim r^{-3}$) density profile is inferred at radii $\gtrsim 6 \times 10^{16}$ cm (see the blue and red density profiles in Figure 5 and the reported values in Table 3). If the second radio flare is a result of an additional delayed outflow with $t_{\rm launch} = 170$ days, then we find a mildly relativistic shock with $v_{\rm sh} \simeq 0.5c$, and no need for density enhancement at large radii. Since the velocity we infer is still only mildly relativistic, the Newtonian formalism is sufficient, and we do not use the

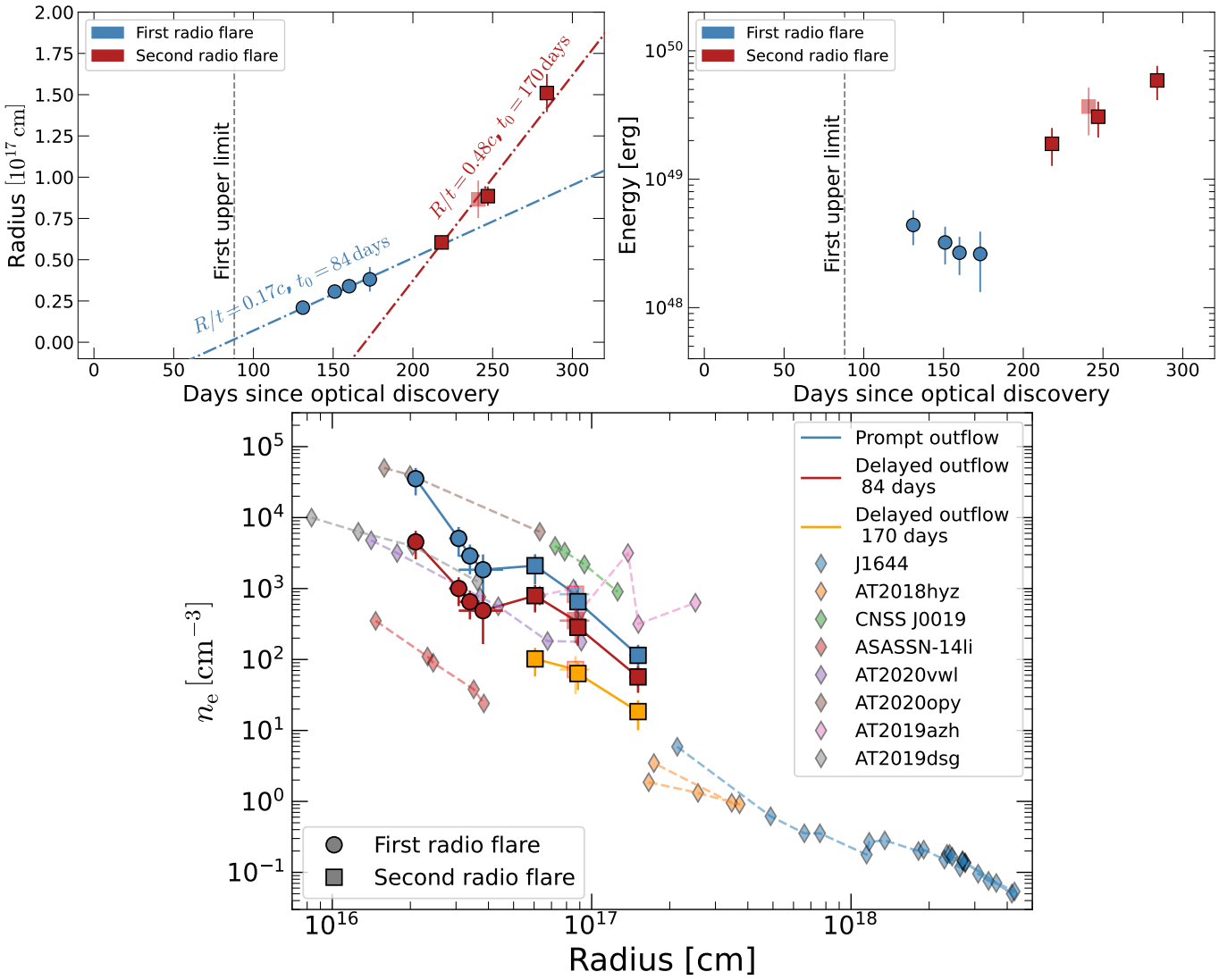

Figure 5. Physical parameters inferred from the fits of the individual SEDs and nonrelativistic equipartition analysis (see Sections 4.1.1 and 4.1.2). The top left panel shows the temporal evolution of the equipartition radius (filled circles for the first flare; filled squares for the second flare). Best-fitting $R(t)$ evolutions for an assumed constant expansion of outflows that were launched at $t_{\rm launch} = 84^{+6}_{-25}$ days and 170 ± 10 days are also plotted (dotted–dashed lines). The top right panel shows the equipartition energy. The bottom panel shows the density profile for an outflow that was launched at time of optical discovery (filled blue circles for the first flare; filled blue squares for the second flare) and for an outflow that was launched 84 days after optical discovery (filled red circles for the first flare; filled red squares for the second flare). In addition, we plot the density profile for a delayed outflow for the second flare only in yellow squares. Also plotted are the density profiles inferred for other radio-bright TDEs. The best-fitting parameters at $\Delta t \simeq 242$ days are marked with a lighter shade to emphasize our uncertainty in the flux measurements of the ATA due to its larger beam.

relativistic formalism discussed in R. Barniol Duran et al. (2013). Finally, we note that in this model the lack of emission at early times, in both radio flares, is purely due to the delayed launching of the outflow(s), and we do not need to invoke FFA. We provide the results of this analysis in Table 3, and we plot the different density profiles in the bottom panel of Figure 5.

4.1.3. Relativistic Jets Observed Off-axis

Another scenario that can explain the emergence of radio emission at late times in TDEs is a relativistic jet that is initially observed off-axis (D. Giannios & B. D. Metzger 2011; P. Beniamini et al. 2023; T. Matsumoto & T. Piran 2023). T. Matsumoto & T. Piran (2023) introduced a generalized equipartition formalism, demonstrating that a relativistic emitter observed off-axis can be disguised as an apparent o n-axis Newtonian outflow. Forward modeling of the synchrotron emission suggested that the peculiar evolution of the radio emission from both Swift J1644+57 (P. Beniamini et al. 2023) and AT 2018hyz (I. Sfaradi et al. 2024) can be a result of a relativistic off-axis jet.[31] In this context, P. Beniamini et al. (2023) derived that the fastest possible observed rise is $F_\nu \sim t^{10}$ (achieved for a flat density profile and a top-hat jet) and the fastest decline is $F_\nu \sim t^{-p}$. These closure relations can explain the fast rise, $F_\nu \gtrsim t^9$, observed in the first flare for $t_{\rm launch} = 0$ days. However, the extremely steep rise of the second flare ($F_\nu \gtrsim t^{18}$) and the declines of both flares ($F_\nu \sim t^{-6}$ and t^{-12} for the first and second flares, respectively) are too fast for an off-axis jet launched promptly after discovery, thus

[31] An on-axis jet but with a wide angular structure carrying more energy than the jet core can also produce a late-time rebrightening similar to that seen in Swift J1644+57 (P. Mimica et al. 2015).

Table 3
Physical Parameters from a Nonrelativistic Equipartition Analysis of Individual SED Fits

	Δt (days)	R (10^{16} cm)	B (G)	β	n_e (cm^{-3})	$U_{\rm ps}$ (erg)
First Radio Flare						
$t_{\rm launch} = 0$ day	131	$2.10^{+0.15}_{-0.12}$	$0.76^{+0.10}_{-0.07}$	$0.062^{+0.005}_{-0.003}$	$(4.0^{+1.6}_{-0.9}) \times 10^4$	$(4.4^{+1.3}_{-0.7}) \times 10^{48}$
	151–154	$3.07^{+0.25}_{-0.22}$	$0.37^{+0.05}_{-0.03}$	$0.078^{+0.007}_{-0.006}$	$(5.8^{+2.5}_{-1.5}) \times 10^3$	$(3.2^{+0.9}_{-0.5}) \times 10^{48}$
	160	$3.39^{+0.31}_{-0.27}$	$0.29^{+0.04}_{-0.03}$	$0.082^{+0.008}_{-0.007}$	$(3.3^{+1.5}_{-0.9}) \times 10^3$	$(2.7^{+0.8}_{-0.5}) \times 10^{48}$
	173	$3.81^{+0.72}_{-0.59}$	$0.24^{+0.05}_{-0.04}$	$0.085^{+0.016}_{-0.013}$	$(2.1^{+2.0}_{-1.0}) \times 10^3$	$(2.6^{+1.2}_{-0.8}) \times 10^{48}$
$t_{\rm launch} = 84$ days	131	⋯	⋯	0.17 ± 0.01	$(5.1^{+2.0}_{-1.2}) \times 10^3$	⋯
	151	⋯	⋯	0.18 ± 0.01	$(1.1^{+0.5}_{-0.3}) \times 10^3$	⋯
	160	⋯	⋯	0.17 ± 0.02	$(7.4^{+3.5}_{-2.1}) \times 10^2$	⋯
	173	⋯	⋯	0.17 ± 0.03	$(5.6^{+5.5}_{-2.7}) \times 10^2$	⋯
Second Radio Flare						
$t_{\rm launch} = 0$ day	218	$6.05^{+0.42}_{-0.40}$	$0.32^{+0.04}_{-0.03}$	$0.107^{+0.008}_{-0.007}$	$(2.4^{+1.0}_{-0.6}) \times 10^3$	$(1.9^{+0.5}_{-0.3}) \times 10^{49}$
	241–242	$8.66^{+1.16}_{-1.07}$	$0.26^{+0.05}_{-0.03}$	0.14 ± 0.02	$(9.6^{+7.0}_{-3.8}) \times 10^2$	$(3.7^{+1.4}_{-0.9}) \times 10^{49}$
	247–248	$8.85^{+0.59}_{-0.55}$	$0.23^{+0.03}_{-0.02}$	0.14 ± 0.01	$(7.5^{+3.0}_{-1.9}) \times 10^2$	$(3.1^{+0.8}_{-0.5}) \times 10^{49}$
	284	15.1 ± 1.1	0.14 ± 0.02	0.21 ± 0.02	$(1.3^{+0.5}_{-0.3}) \times 10^2$	$(5.9^{+1.4}_{-0.9}) \times 10^{49}$
$t_{\rm launch} = 84$ days	218	⋯	⋯	0.17 ± 0.01	$(9.1^{+3.7}_{-2.3}) \times 10^2$	⋯
	241–242	⋯	⋯	0.21 ± 0.03	$(4.1^{+3.0}_{-1.6}) \times 10^2$	⋯
	247–248	⋯	⋯	0.21 ± 0.01	$(3.3^{+1.3}_{-0.8}) \times 10^2$	⋯
	284	⋯	⋯	0.29 ± 0.02	65^{+26}_{-17}	⋯
$t_{\rm launch} = 170$ days	218	⋯	⋯	0.49 ± 0.03	$(1.3^{+0.5}_{-0.3}) \times 10^2$	⋯
	241–242	⋯	⋯	0.47 ± 0.06	83^{+61}_{-33}	⋯
	247–248	⋯	⋯	0.44 ± 0.03	73^{+29}_{-19}	⋯
	284	⋯	⋯	0.51 ± 0.04	21^{+9}_{-6}	⋯

Note. The physical parameters of the outflows and their environment based on the broken power-law fits to the individual radio SEDs (Sections 4.1, 4.1.1, and 4.1.2) are listed. The radius and magnetic field strength are calculated using Equations (1) and (2), respectively. The normalized velocity, β, is defined by $R/(\Delta t - t_{\rm launch}) \equiv \beta c$. The number density is calculated using Equation (3). The last column is of the post-shock equipartition energy, and it is calculated using Equation (5). Since the radius, magnetic field, and equipartition energy are not time dependent, we do not repeat these values for different $t_{\rm launch}$ (this is marked with "–"). These reported values assume $\epsilon_e = \epsilon_B = 0.1$, and $f = 0.5$.

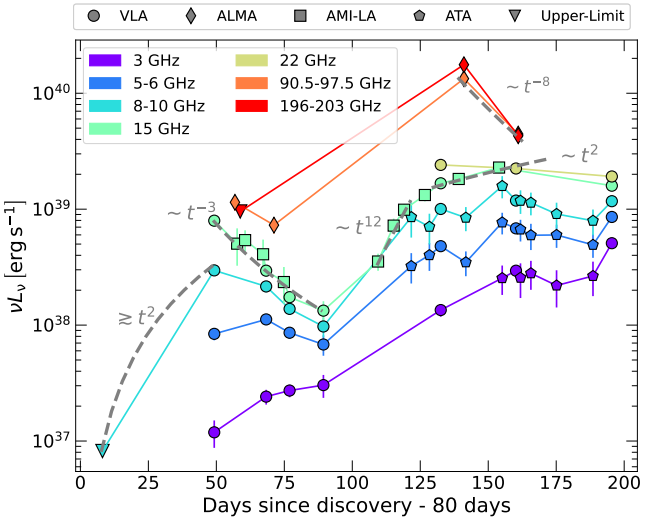

Figure 6. Radio light curves of AT 2024tvd as in Figure 3 with power-law evolution for $t_{\rm launch} = 80$ days.

requiring $t_{\rm launch} > 0$ days in both cases. We set $t_{\rm launch}$ based on the requirement that the emission decline at most as steeply as $F_\nu \sim t^{-3}$, and we note that this is a conservative approach, as the emission is expected to follow $F_\nu \sim t^{-p}$, and we observe $p \simeq 2.15$ for both flares. This approach results in $t_{\rm launch} \gtrsim 80$ days for the first flare and $t_{\rm launch} \gtrsim 190$ days for the second flare. For reference, in Figure 6 we present the radio light curves with the temporal indices for the case of $t_{\rm launch} \simeq 80$ days.

We explore the possibility of an off-axis jet model by generalizing the method devised by T. Matsumoto & T. Piran (2023). In this model, the observables are transformed from the rest-frame quantities by the relativistic Doppler factor $\delta_{\rm D} \equiv \frac{1}{\Gamma(1-\beta\cos\theta)}$, where $\Gamma \equiv \frac{1}{\sqrt{1-\beta^2}}$ and θ is the angle between the direction of motion of the jet and the line of sight of the observer. R. Barniol Duran et al. (2013) generalized equipartition analysis by accounting for electrons that radiate at ν_m. This introduces additional factors that arise from the fact that the energy of the electrons is higher (see discussion in their Section 4.2.1). We generalize the T. Matsumoto & T. Piran (2023) derivation by accounting for these electrons and for a general power-law index of the relativistic electrons, p. We find the following (a full derivation is in Appendix D):

$$R_{\rm eq} = (10^{17}\,{\rm cm})[159 \times [520]^{p-1}]^{\frac{1}{2p+13}} \times F_{p,{\rm mJy}}^{\frac{p+6}{2p+13}} d_{L,28}^{\frac{2(p+6)}{2p+13}} \nu_{p,10}^{-1} (1+z)^{-\frac{3p+19}{2p+13}} \epsilon^{\frac{1}{2p+13}} \times \gamma_m^{\frac{2-p}{2p+13}} f_A^{-\frac{p+5}{2p+13}} f_V^{-\frac{1}{2p+13}} \Gamma \delta_D^{-\frac{p+5}{2p+13}} \xi^{\frac{1}{2p+13}}, \quad (6)$$

$$E_{\rm eq} = (3.36 \times 10^{48}\ {\rm erg})[159]^{-\frac{2(p+1)}{2p+13}}[520]^{\frac{11(p-1)}{2p+13}} \times F_{p,{\rm mJy}}^{\frac{3p+14}{2p+13}} d_{L,28}^{\frac{2(3p+14)}{2p+13}} \nu_{p,10}^{-1}(1+z)^{-\frac{5p+27}{2p+13}} \times \left[1+\left(\frac{2p+2}{11}\right)\epsilon\right]\epsilon^{\frac{-2(p+1)}{2p+13}}\gamma_m^{\frac{11(2-p)}{2p+13}} f_A^{-\frac{3(p+1)}{2p+13}} \times f_V^{\frac{2(p+1)}{2p+13}}\Gamma\delta_D^{-\frac{7p+29}{2p+13}}\xi^{\frac{11}{2p+13}}, \quad (7)$$

where $F_{p,{\rm mJy}}$ is the peak flux density in mJy; $d_{L,28}$ is the luminosity distance normalized to 10^{28} cm; $\nu_{p,10}$ is the observed peak frequency normalized to 10 GHz; z is the redshift to the source; f_A and f_V are the area and volume filling factors, respectively; $\epsilon \equiv (\epsilon_B/\epsilon_e)/\left(\frac{2p+2}{11}\right)$; and $\xi \equiv 1 + \epsilon_e^{-1}$. For this relativistic case we consider $\gamma_m = \max\left[2,\ \epsilon_e \frac{p-2}{p-1}\frac{m_p}{m_e}(\Gamma - 1)\right]$ as the minimal Lorentz factor of the radiating electrons.

To derive the physical parameters of an off-axis jet, we follow the same procedure outlined in T. Matsumoto & T. Piran (2024) and C. T. Christy et al. (2024). The radius, R, and the time of observation since the jet was launched, t, are related by the time measured with a photon emitted by a relativistically moving source with normalized velocity β at an angle θ,

$$t = \frac{(1+z)R}{c\beta}(1 - \beta\cos\theta). \quad (8)$$

We then solve numerically for the radius in Equations (6) and (8) for viewing angles $\theta = 30°, 45°, 60°$, and 90°. For the surrounding density profile we assume a strong shock, i.e., $n_e = \frac{N_e}{4V}$, where N_e is the number of emitting electrons (Equation (D2)) and $V \equiv f_V \pi R_{\rm eq}^3/\Gamma^4$ is the emitting volume. We assume $f_A = f_V = 1$, which accounts only for energy within $1/\Gamma$ from our line of sight.

We note that for an assumed $\epsilon_{\rm e} = 0.1$ the large Lorentz factors we infer for some of the viewing angles result in $\nu_{\rm sa} < \nu_m, \nu_c$, which is not consistent with our observations (we find a steeper spectral slope in the optically thick regime than all the cases discussed in J. Granot & R. Sari 2002 with $\nu_{\rm sa} < \nu_{\rm m}$). Our observations imply $\nu_m \lesssim 1.5\ {\rm GHz} < \nu_{\rm sa}$, and, in order to be self-consistent, we rederive the generalized equipartition formalism introduced in T. Matsumoto & T. Piran (2023) for the correct frequency ordering (Appendix D) and add the requirement of $\nu_m \lesssim 1.5$ GHz. We note that this requirement is necessary, as we do not observe the actual position of ν_m, and therefore we assume that it is below our observing range. The inferred ϵ_e are thus upper limits in this case. Finally, we also assume equipartition, $\epsilon_e = \epsilon_B$. The results of this analysis are shown in Figure 7 and summarized in Table 4.

For the first radio flare we find that a relativistic jet launched ~80 days after optical discovery at $\theta \simeq 60°$–$90°$ can explain the observed emission with moderate Lorentz factors and density profiles similar to those seen in other radio-bright TDEs. Smaller viewing angles require larger Γ and density profiles: for $\theta = 30°$ we find $\Gamma \sim 30$ and a density profile ~3–4 orders of magnitude larger than seen in Swift J1644+57 at radii $\gtrsim 10^{18}$ cm (see top panels of Figure 7).

For the second radio flare we infer $t_{\rm launch} = 190$ days (based on the requirement of $F_\nu \sim t^{-3}$ in the optically thin regime), which is only ~4 days before the first detection of the second radio flare. Therefore, any relativistic jet has to be either only slightly off-axis or only mildly relativistic for us to see it that soon (see bottom panels of Figure 7). Overall we find moderate Lorentz factors, $\Gamma \leqslant 10$, and densities $n_e \lesssim 100$ up to $\sim 10^{18}$ cm for all the viewing angles we have tested. By relaxing the requirement of a delayed jet for the second flare and assuming a prompt off-axis jet, we infer $\Gamma > 10$ and $E_{\rm eq} \gtrsim 10^{51}$ erg for $\theta < 60°$. In this scenario, an extreme density profile of $\rho \sim r^{-15}$ is inferred. Therefore, we conclude that an off-axis relativistic jet launched around the time of optical discovery is disfavored.

4.2. Multiepoch Time-dependent Modeling of the First Radio Flare

We next refine our nonrelativistic analysis by adopting a time-dependent model to fit the emission from the first radio flare only, and we show that it can be explained by a shock wave interacting with a single power-law density profile. We attempted the same approach for the second flare. However, more epochs of observations are needed to constrain the evolution of the optically thin regime. We leave the modeling of the second radio flare beyond equipartition for future work.

We assume that the emission is from a shock wave traveling with roughly constant velocity, $r(\Delta t) = \beta_0 c(\Delta t - t_{\rm launch})$, and interacting with a single power-law density profile $n_e(r) = n_0(r/r_0)^{-k}$, where $r_0 \equiv \beta_0 c(\Delta t_0 - t_{\rm launch})$, and we choose $\Delta t_0 = 131$ days as our reference time (the time of the first radio detection).[32] We use the model presented in Appendix C to self-consistently calculate the different synchrotron break frequencies, and specifically Equation (C11) to calculate F_p and ν_p. We then use Equation (4) to calculate the SED shape before and after the spectral peak. The shape parameter around the peak, s, is defined for each transition in J. Granot & R. Sari (2002). We use sharp breaks for other spectral breaks that are not around the peak, and we follow the power-law indices discussed in J. Granot & R. Sari (2002). This results in a self-absorbed synchrotron spectrum $F_{\nu,\,{\rm ssa}}(t)$. We also calculate the FFA optical depth as in G. B. Rybicki & A. P. Lightman (1986; see also A. J. Nayana et al. 2025):

$$\tau_{\rm FFA}(r,\,\nu) = \int_r^\infty 0.018 \times T_e^{-3/2} Z^2 \nu^{-2} g_{\rm ff} n_e^2(r')dr', \quad (9)$$

where T_e is the temperature of the electrons in the surrounding medium, we use a Gaunt factor $g_{\rm ff} = 5$ and a charge of $Z = 1$, and we assume full ionization of the medium. We then calculate $\nu_{\rm ff}$ by setting $\tau_{\rm FFA}(r,\,\nu_{\rm ff}) \equiv 1$. The resulting spectrum is given by $F_\nu(t) = F_{\nu\ {\rm ssa}}(t) \times e^{-\tau_{\rm FFA}} = F_{\nu\ {\rm ssa}}(t) \times e^{-(\nu/\nu_{\rm ff})^{-2}}$. Finally, we also account for the effects of IC cooling by thermal optical/UV photons. IC cooling effects are typically neglected in the TDE literature. However, they are relevant for the first radio flare, as the thermal emission from the TDE is still bright.

We fit this model to all of the radio data from the first flare (up to $\Delta t \leqslant 173$ days) assuming $t_{\rm launch} = 84$ days.[33] The free parameters are β_0, n_0, k, p, and ϵ_B. In this fitting process we fit

[32] Note that we find in our analysis $k > 3$. This steep profile should lead to an acceleration of the shock wave (E. Waxman & D. Shvarts 1993). However, for simplicity, we do not account for this acceleration and assume constant expansion. We leave the introduction of more complicated hydrodynamics to future work.

[33] We note that a prompt outflow leads to inconsistencies with the data when IC cooling is accounted for (see Appendix A). Therefore, we assume a delayed outflow and use $t_{\rm launch}$ inferred based on the equipartition analysis in Section 4.1.2.

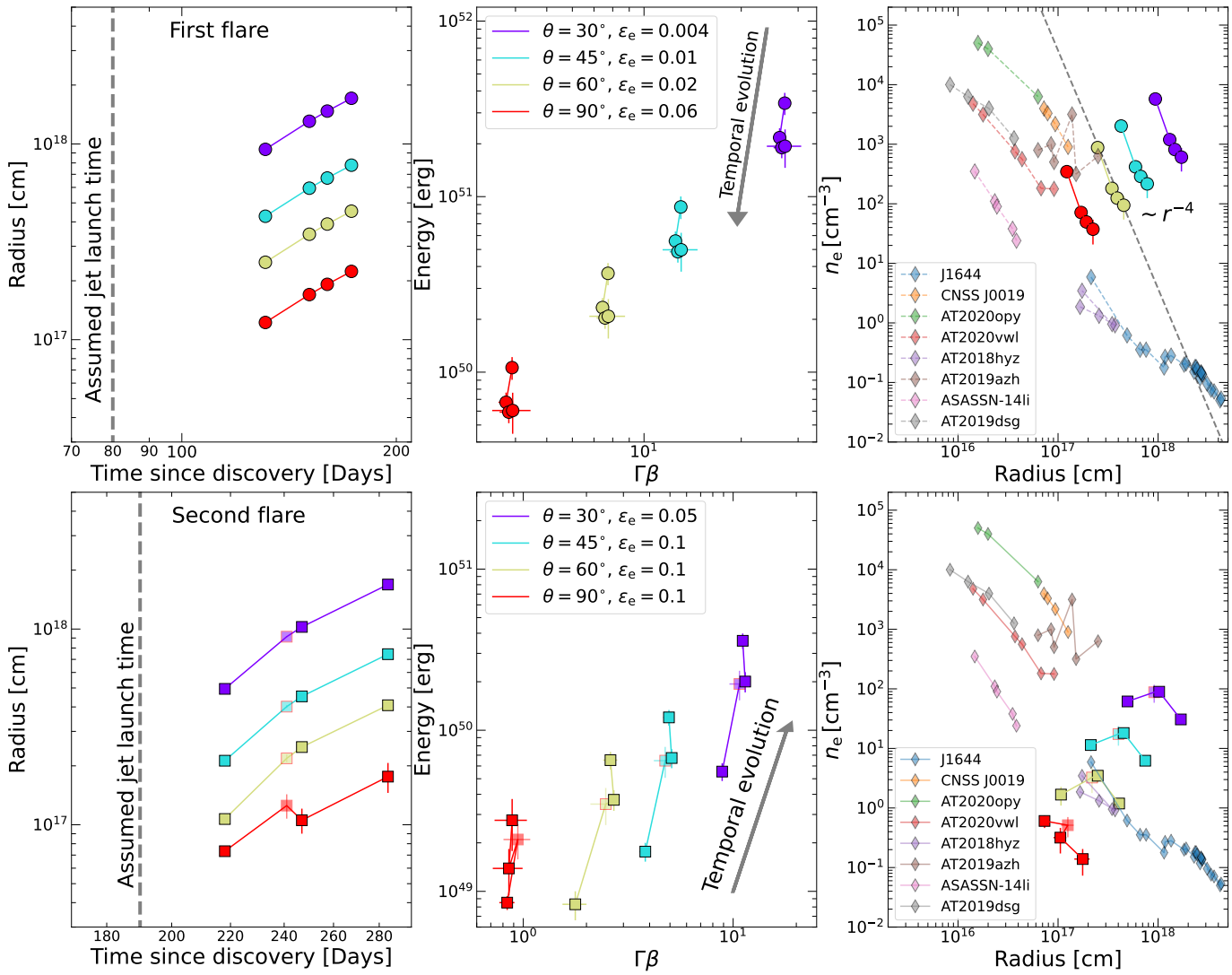

Figure 7. Physical parameters from the generalized equipartition analysis of a relativistic off-axis jet. The top panels show the results for the first radio flare, assuming $t_{\rm launch} = 80$ days, and the bottom panels show the results for the second radio flare for $t_{\rm launch} = 190$ days. The left panels show the evolution of the radius with time, the middle panels show the equipartition energy vs. proper velocity (we mark the temporal evolution with an arrow), and the right panels display the inferred density profile compared to other radio-bright TDEs. We show the results of this analysis for observer angles of $\theta = 30°$, 45°, 60°, and 90°. For each observing angle we use the largest ϵ_e (up to $\epsilon_e = 0.1$) that satisfies the relation $\nu_m \leqslant 1.5$ GHz in all of our epochs (see discussion in Section 4.1.3).

for the synchrotron cooling frequency and check that our results are consistent with the location of the IC cooling frequency, $\nu_{\rm IC}$, based on the optical/UV luminosity (Y. Yao et al. 2025, in preparation) and the Lorentz factor of the IC cooling (Appendix A). We do not fit for $\nu_{\rm IC}$ in our fitting process, as the uncertainty of the optical/UV luminosity translates to high uncertainties on the fitted parameters.

We further assume that the temperature of the electrons in the surrounding medium is $T_e = 10^5$ K, filling factors of $f_A = 1$, and $f = 0.5$. We also assume[34] $\epsilon_e = 0.001$ since there is a degeneracy between ϵ_e and ϵ_B. We use `emcee` to determine the best-fitting parameters and infer their posterior distribution. We use the following flat priors: $0.005 < \beta_0 < 0.9$, $1 < \log_{10}(n_0/[\rm cm^{-3}]) < 11$, $1 < k < 9$, $\log_{10}(2.001) < \log_{10}(p) < \log_{10}(3)$, and $-7 < \log_{10}(\epsilon_{\rm B}) < \log_{10}(0.33)$. We use 200 walkers with 30,000 steps for each chain and discard the first 1000 steps for burn-in. We plot the different SEDs and the 10 GHz light curve together with lines drawn from the resulting posterior distribution in Figure 8.

We find that this approach accounts for all of the nontrivial observables of the first radio flare. The early 10 GHz upper limit is easily explained by the combination of FFA and the delayed outflow. The late emergence of the radio emission and the unprecedentedly fast evolution of the radio spectral peak is explained by a rather steep density profile of $n(r) = n_0(r/r_0)^{-3.8\pm0.1}$ (see the best-fitting density profile in the bottom right panel of Figure 8). We also find $n_0 = 10^{5.2\,\pm\,0.2}\,\rm cm^{-3}$ at $r_0 \simeq 2.1 \times 10^{16}$ cm (see a summary of the model parameters in Table 5). In addition, the change in the optically thin spectral index between the first and second epochs of our ALMA observations is naturally explained as the result of the synchrotron cooling frequency evolving from $\sim$50 GHz to $\nu_c \gtrsim 100$ GHz at later times. Finally, since our millimeter-band observations constrain the evolution of the cooling frequency, our fit constrains ϵ_B for the given

[34] We can also fit the data when assuming $\epsilon_e = 0.01$; however, the assumption of $\epsilon_e = 0.001$ provides better constraints on p. We note that increasing ϵ_e by an order of magnitude increases ϵ_B and decreases the density by an order of magnitude while keeping all other physical parameters the same.

Table 4
Physical Parameters Derived from the Relativistic Off-axis Equipartition Analysis of Individual SED Fits (Section 4.1)

	Δt (days)	$R_{\rm eq}$ (10^{17} cm)	$E_{\rm eq}$ (erg)	$\Gamma\beta$	n_e (cm^{-3})
			First Radio Flare	$-t_{\rm launch} \equiv 80$ days	
$\theta = 45°$	131	4.27 ± 0.01	$(8.7 \pm 1.0) \times 10^{50}$	13.0 ± 0.4	$(2.0 \pm 0.4) \times 10^3$
$\epsilon_e = \epsilon_B = 0.01$	151–154	5.94 ± 0.01	$(5.6 \pm 0.7) \times 10^{50}$	12.5 ± 0.6	$(4.2^{+0.9}_{-0.7}) \times 10^2$
	160	6.70 ± 0.01	$(4.9^{+0.7}_{-0.6}) \times 10^{50}$	12.7 ± 0.7	$(2.8^{+0.6}_{-0.5}) \times 10^2$
	173	7.79 ± 0.02	$(5.0 \pm 1.0) \times 10^{50}$	13.0 ± 1.6	$(2.2^{+1.0}_{-0.7}) \times 10^2$
$\theta = 90°$	131	1.23 ± 0.01	$(1.1 \pm 0.2) \times 10^{50}$	3.90 ± 0.15	$(3.5^{+0.7}_{-0.6}) \times 10^2$
$\epsilon_e = \epsilon_B = 0.06$	151–154	1.70 ± 0.01	$(6.7 \pm 0.9) \times 10^{49}$	3.7 ± 0.2	71^{+15}_{-13}
	160	1.92 ± 0.01	$(5.9 \pm 0.8) \times 10^{49}$	3.8 ± 0.2	49^{+11}_{-10}
	173	2.23 ± 0.02	$(6.0 \pm 1.5) \times 10^{49}$	3.9 ± 0.5	37^{+17}_{-13}
			Second Radio Flare	$-t_{\rm launch} \equiv 190$ days	
$\theta = 45°$	218	2.12 ± 0.03	$(1.8 \pm 0.2) \times 10^{49}$	3.8 ± 0.2	11 ± 2
$\epsilon_e = \epsilon_B = 0.1$	241–242	4.0 ± 0.07	$(6.5 \pm 1.0) \times 10^{49}$	4.7 ± 0.6	17 ± 6
	247–248	4.53 ± 0.03	$(6.7^{+1.0}_{-0.8}) \times 10^{49}$	5.1 ± 0.3	18^{+4}_{-3}
	284	7.44 ± 0.06	$(1.2 \pm 0.1) \times 10^{50}$	4.9 ± 0.3	6 ± 1
$\theta = 90°$	218	0.73 ± 0.01	$(8.5 \pm 0.8) \times 10^{48}$	0.84 ± 0.07	0.6 ± 0.1
$\epsilon_e = \epsilon_B = 0.1$	241–242	$1.35^{+0.04}_{-0.34}$	$(2.1^{+0.4}_{-0.8}) \times 10^{49}$	0.94 ± 0.15	0.5 ± 0.2
	247–248	$1.05^{+0.34}_{-0.05}$	$(1.4^{+0.8}_{-0.2}) \times 10^{49}$	$0.8^{+0.2}_{-0.1}$	$0.3^{+0.2}_{-0.1}$
	284	$1.7^{+0.6}_{-0.1}$	$(2.8^{+1.6}_{-0.6}) \times 10^{49}$	0.9 ± 0.2	$0.14^{+0.07}_{-0.05}$

Note. Physical parameters of a relativistic off-axis jet and its environment based on the broken power-law fits of individual radio SEDs and the generalized equipartition analysis described in Section 4.1.3 and Appendix D. We report here the values for observing angles of 45° and 90° (Figure 7 also shows the results for $\theta = 30°$ and 60°). We set different launch times of the jet for the first and second flares based on the requirement that the decline of the radio emission will not exceed $F_\nu \sim t^{-3}$. We report here the largest value of ϵ_e (up to $\epsilon_e = 0.1$) that satisfies the condition $\nu_m < 1.5$ GHz (see details in Section 4.1.3).

$\epsilon_e = 0.001$. We find $\log_{10}(\epsilon_B) = -1.9 \pm 0.3$, implying deviation from equipartition. In the bottom left panel of Figure 8 we plot the evolution of $\nu_{\rm sa}$, $\nu_{\rm sync}$, and $\nu_{\rm ff}$. The cooling frequency is $\nu_c = \min[\nu_{\rm sync}, \nu_{\rm IC}]$, and our model is consistent with $\nu_{\rm sync} \simeq \nu_{\rm IC}$ (within 1σ uncertainty) in all epochs for which we observe a cooling spectral break in the optically thin regime. Therefore, we conclude that our model is self-consistent with the location of the IC cooling frequency even though we are not explicitly accounting for it in our fitting process. On the other hand, we explicitly account for it when we apply the same model for a prompt outflow (which we disfavor because of the required high energetics and densities; see Appendix A).

5. Discussion

The radio emission from the first radio-bright off-nuclear TDE AT 2024tvd exhibits two rapidly evolving radio flares at late times, with the following main features in order:

1. An initial deep upper limit, $\nu L_\nu \leqslant 8 \times 10^{36}$ erg s^{-1}, about 88 days after optical discovery, followed by bright radio emission, $\nu L_\nu \sim 3 \times 10^{38}$ erg s^{-1}, at $\Delta t = 131$ days.
2. A fast decline of the broadband SED, with a peak flux that evolves as $F_p \sim t^{-6}$ between 131 and 173 days after optical discovery.
3. The transition of the cooling frequency from $\sim$50 GHz at $\Delta t = 131$–141 days to $\gtrsim$100 GHz at $\Delta t \simeq 154$ days.
4. Fast rebrightening at $\Delta t = 194$ days, initially rising as $F_\nu \sim t^{18}$ in the centimeter bands, and a fast decay, $F_\nu \sim t^{-12}$, of the millimeter-band emission.
5. A rise of the peak flux density of the broadband SED in the range of $\Delta t = 218$–284 days, accompanied by a decline of the peak frequency.

The radio emission from AT 2024tvd stands out compared to other radio-bright TDEs. Some TDEs, most notably ASASSN-15oi (A. Horesh et al. 2021a; A. Hajela et al. 2025) and AT 2020vwl (A. J. Goodwin et al. 2023, 2025b), also exhibit two distinct radio flares. For both ASASSN-15oi and AT 2020vwl, the separation in time between the two flares is significantly larger than what we observe for AT 2024tvd, and their radio emission evolves on a much longer timescale (see Figure 2). A fast rise is also observed for the late-time component of AT 2019azh (I. Sfaradi et al. 2022). However, it is fainter than both flares of AT 2024tvd, and it is present in addition to a prompt emission component (A. J. Goodwin et al. 2022). Another notable example is ASASSN-19bt, in which a transition in the spectral evolution is observed and associated with either one outflow interacting with a complex CNM or two distinct outflows (C. T. Christy et al. 2024).

The peculiar evolution of the radio emission from AT 2024tvd, and specifically the emergence of two late-time radio flares, raises the following questions: (1) Can a single outflow produce both flares? (2) When and why were the radio-emitting outflow(s) launched? (3) What is the nature of these outflows (i.e., spherical nonrelativistic outflow vs. relativistic jet)? We address these questions in the following discussion (a summary of the possible scenarios is reported in Table 6).

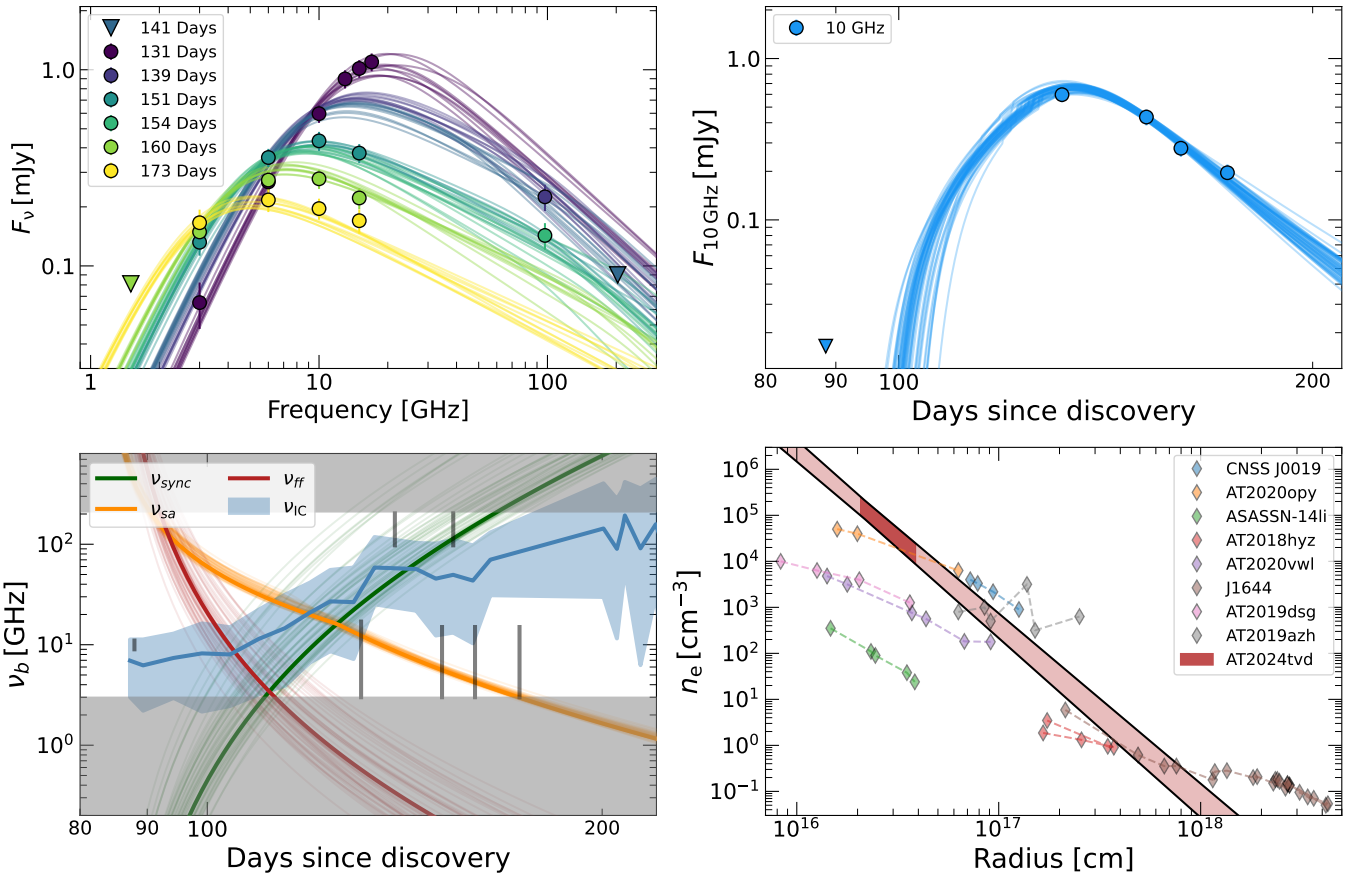

Figure 8. Results from the time-dependent model applied to the first radio flare, for $t_{\rm launch} = 84$ days. The top left panel shows the broadband SEDs, with models drawn from the posterior distributions obtained by using `emcee`. The top right panel is for the 10 GHz light curve, with lines drawn from the posterior distributions. The evolution of the broadband SED, and especially the change of the optically thin spectral slope, can be easily explained by the transition of the cooling break frequency from ∼60 GHz around $\Delta t = 131$ days to $\gtrsim$100 GHz at $\Delta t \gtrsim 154$ days. The bottom left panel presents the temporal evolution of the synchrotron break frequencies ($\nu_m < 0.1$ GHz at all times and is not displayed here). The black vertical lines represent the range of observed frequencies at each time. We note that while we do not fit for $\nu_{\rm IC}$, represented here in a blue region based on the best-fitted parameters and the optical/UV luminosity, our observations are consistent, within 1σ uncertainties with its temporal evolution. Finally, the bottom right panel displays the density profile around AT 2024tvd compared to other radio-bright TDEs (marked with colored diamonds). The density profile we infer for AT 2024tvd is marked with a red shaded region (marking 1σ uncertainty); a lighter shade is for the extrapolated radii.

5.1. The Nature of the First Radio Flare

Newtonian equipartition analysis of the emission from the first radio flare suggests that for an outflow that was launched promptly after the optical discovery the shock is accelerating. The shock velocities we infer in this case are ∼0.06c–0.085c, and they are in agreement with the velocities expected from accretion-driven winds and the unbound tidal debris stream (L. E. Strubbe & E. Quataert 2009; J. Krolik et al. 2016; K. D. Alexander et al. 2020; C. Bonnerot & W. Lu 2020). However, a prompt outflow from AT 2024tvd requires an extremely high post-shock energy, of a few $\times\ 10^{52}$ erg, and CNM densities, $n_e \sim 2 \times 10^7\,{\rm cm}^{-3}$ at $\sim 3 \times 10^{16}$ cm (see Appendix A). Instead, our time-dependent analysis suggests that a delayed Newtonian outflow, launched at $t_{\rm launch} = 84^{+6}_{-25}$ days, naturally explains all emission features without invoking extreme energetics and densities, thus favoring the delayed outflow scenario in the context of nonrelativistic ejecta.

Physically, a delayed emergence of the radio emission might arise from a relativistic jet that initially points away from our line of sight (e.g., T. Matsumoto & T. Piran 2023; I. Sfaradi et al. 2024, in the context of TDEs). However, in this scenario it is challenging to explain the fast decay of $F_\nu \sim t^{-6}$ with the expected $F_\nu \sim t^{-p}$ (P. Beniamini et al. 2023), which would imply a nonphysical spectral slope of $p \approx 6$. Therefore, we find that a prompt off-axis jet is an unlikely scenario. We estimate that the earliest outflow launch time for an off-axis jet is at $\Delta t \approx 80$ days (by requiring $F_\nu \sim t^{-3}$), similar to the inferred $t_{\rm launch}$ for a nonrelativistic outflow. In this context, we favor $\theta \gtrsim 60°$, as smaller viewing angles require higher Lorentz

Table 5
Physical Parameters of the Time-dependent Model for the First Radio Flare

Parameter	Definition	Value
$t^{\dagger}_{\rm launch}$	Outflow launch time [days]	84
$t^{\dagger}_0$	Normalization time [days]	131
β_0	Velocity normalized by c	0.17 ± 0.01
$r_0 \equiv \beta_0 t_0$	Radius at t_0[10^{16} cm]	2.1 ± 0.1
n_0	Density at r_0[cm^{-3}]	$10^{5.2 \pm 0.2}$
k	PL index of the density	-3.8 ± 0.1
p	PL index of the electrons	2.15 ± 0.10
$\epsilon_{\rm B}$	Energy fraction in the B fields	$10^{-1.9 \pm 0.3}$
$\epsilon^{\dagger}_e$	Energy fraction in the electrons	10^{-3}

Note. The model parameters of the time-dependent model described in Section 4.2. Parameters marked with † are fixed in our modeling. Note that r_0 is not fitted in our model but evaluated assuming constant expansion.

Table 6
A Summary of the Different Possible Scenarios for Each Radio Flare

	First Radio Flare	Second Radio Flare
Prompt nonrelativistic outflow	Requires high densities ($n_e \approx 2 \times 10^7$ cm^{-3} at 3×10^{16} cm) and post-shock energy (a few $\times$ 10^{52} erg) to explain the early upper limit and the fast evolution of the broadband SED; therefore, it is disfavored.	The observed fast rise and decay of the radio emission require either a density cavity or larger densities than those inferred for the first radio flare at small radii (producing FFA). We conclude that this scenario is disfavored.
Prompt relativistic outflow	Does not explain the $F_\nu \sim t^{-6}$ decay and requires an unphysically steep spectral slope of $p \approx 6$. Therefore, it is unlikely that the first radio flare is a result of a prompt relativistic off-axis jet, and we conclude that this scenario is disfavored.	The temporal power laws are extremely fast ($F_\nu \sim t^{18}$ during the rise and $F_\nu \sim t^{-12}$ in the optically thin regime) and do not follow the closure relations for a prompt off-axis jet. Therefore, this scenario is disfavored.
Delayed nonrelativistic outflow	An outflow launched at $t_{\rm launch} \approx 84$ days can easily explain the initial upper limit and the fast evolution of the radio emission. This scenario requires a relatively steep density profile, $n_e \sim r^{-3.8}$, but with densities similar to other radio-bright TDEs. We find this scenario to be possible.	There are two possible scenarios of a delayed outflow: (1) the same outflow that produced the first radio flare launched at $t_{\rm launch} \approx 84$ days and interacting with a complex density profile, and (2) a second, mildly relativistic, delayed outflow launched at $t_{\rm launch} \approx 170$ days. We conclude that both of these scenarios are possible.
Delayed relativistic outflow	To achieve a decline of $F_\nu \sim t^{-3}$, we require $t_{\rm launch} \sim 80$ days. In this scenario, an observing angle of $\theta \gtrsim 60°$ is more likely based on the inferred high densities for lower observing angles. Therefore, we find this scenario to be possible.	To achieve a decline of $F_\nu \sim t^{-3}$, we require $t_{\rm launch} \sim 190$ days. This scenario requires fine-tuning of the jet launching time and the physical parameters for us to observe it, and we find it to be possible but less likely than the nonrelativistic scenario.

factors and higher densities, which are less physical at the inferred large radii (see top panel of Figure 7).

Overall, our analysis points at a delayed outflow (either nonrelativistic or ultrarelativistic), launched at $\Delta t \sim 80$ days for the origin of the first radio flare. Interestingly, the X-ray analysis conducted by Y. Yao et al. (2025b) concluded that the X-ray emission during the first ∼80 days is best described by a thermal multitemperature disk model with no evidence for a Comptonization component. A Comptonization component emerges at $\Delta t \gtrsim 80$ days (see Figure 5 in Y. Yao et al. 2025b). We find it intriguing that the onset of a detectable Comptonization in the X-rays is roughly simultaneous with the inferred radio outflow launching time, and we speculate that the origin of the first radio flare is an accretion-driven outflow. Thermal X-ray emission from TDEs is typically associated with the accretion around the MBH. Therefore, it is possible that the spectral change in the X-ray emission is related to the accretion state of the disk. A disk–outflow relation is used to explain the observed radio–X-ray connection for X-ray binaries (XRBs; R. P. Fender et al. 2004). There, the emergence of optically thin radio emission is associated with a jet launched following a transition in the accretion state seen in the X-rays. In some cases discussed in the context of XRBs, the Comptonization component in the hard X-rays can be a result of upscattering of thermal disk photons by a hot e^- corona and/or dynamical Comptonization by infalling material (e.g., L. Titarchuk & E. Seifina 2021). If the emergence of the nonthermal X-ray component is due to the latter, a fraction of the infalling material can result in an outflow. Finally, a disk–outflow connection was also proposed for TDE accretion disks at late times when the accretion rate decreases below $\sim 0.03 \dot{M}_{\rm Edd}$ (D. Giannios & B. D. Metzger 2011). However, the inferred outflow launch day ($\Delta t \sim 80$ days) is probably too early for the accretion rate to drop to these sub-Eddington values.

5.2. The Nature of the Second Radio Flare

The origin of the second radio flare is difficult to explain with a prompt outflow scenario (both nonrelativistic and relativistic), as it was first detected at $\Delta t \approx 194$ days and initially rose as fast as $F_\nu \sim t^{18}$ (with a transition to $F_\nu \sim t^4$ about a month later). A prompt nonrelativistic outflow would require either large densities at $R \leqslant 6 \times 10^{16}$ cm to explain the late turn-on of the radio emission with absorption in front of the shock suppressing the radio emission or a density cavity at these radii. In addition, a density enhancement at $R \geqslant 6 \times 10^{16}$ cm is needed if both radio flares are from the same nonrelativistic outflow (in the equipartition formalism). Therefore, the second radio flare is less likely to be a result of a prompt nonrelativistic outflow. On the other hand, the observed increase in the equipartition energy and the fast evolution of the optically thin emission can also be explained by an off-axis relativistic jet, as emission from more parts of the jet is entering our line of sight at late times (see, e.g., Swift J1644+57; P. Beniamini et al. 2023, AT 2018hyz; I. Sfaradi et al. 2024). However, we find that even for an off-axis jet $t_{\rm launch} \simeq 190$ days is needed to match $F_\nu \sim t^{-3}$ in the optically thin regime. This is only ∼4 days before the first radio detection of this flare. Therefore, we conclude that in the of f-axis jet scenario either the jet is only mildly relativistic, if it is significantly off-axis ($\Gamma\beta \lesssim 1$ for $\theta \approx 90°$), or, if the jet is ultrarelativistic, it is only slightly off-axis ($\Gamma \simeq 12$ for $\theta \approx 30°$). Although we find this scenario possible, we note that it requires some fine-tuning of the physical parameters.

Analysis of the broadband SEDs of the second flare in the Newtonian limit results in a radio-emitting outflow at larger radii than the radii inferred for the first flare (for a nonrelativistic outflow). In addition, the first estimation of the equipartition radius during this second flare is consistent with the temporal evolution of the equipartition radius during the first radio flare. Therefore, it is possible that a single outflow is producing both radio flares. The inferred density profile in a single outflow scenario, assuming $t_{\rm launch} = 84^{+6}_{-25}$ days (which is the preferred

outflow launch time), points to a flattening of the density profile followed by a shallower density profile. For this reason, we consider the possibility that the rebrightening of the radio emission is due to one delayed outflow interacting with a complex density profile (as was previously suggested by T. Matsumoto & T. Piran 2024). Alternatively, it is also possible that a second outflow was launched at $t_{\rm launch} = 170 \pm 10$ days. A higher shock velocity of $\sim 0.5c$ is needed for such an outflow, as well as lower densities, roughly matching the extrapolation of the first delayed radio flare in the framework of the equipartition analysis, but with a shallower profile of $n_e \sim r^{-2}$.

Overall, our analysis of the emission from the second flare favors either (1) a scenario in which the same outflow that was launched around $t_{\rm launch} \approx 80$ days is interacting with a complex density profile or (2) a scenario of a second distinct outflow launched at $t_{\rm launch} \approx 170$ days for a subrelativistic outflow or at $t_{\rm launch} \approx 190$ days for a relativistic outflow. We note that the high-GHz emission observed with ALMA at $\Delta t = 227$ days is too high compared to the low-GHz emission, and we cannot account for it in our equipartition analysis. We leave the analysis of this emission to future time-dependent modeling. While observations are still being acquired and we defer a full time-dependent modeling of the second flare to a later letter, we discuss the astrophysical implications of our findings below.

5.3. Astrophysical Implications

AT 2024tvd is the first bona fide off-nuclear TDE with extensive radio coverage, and it also exhibits one of the most peculiar radio light curves observed for a TDE to date. We raise here the possibility that the unique radio evolution is related to the off-nuclear position of the MBH and to the possible IMBH TDE scenario (Y. Yao et al. 2025b inferred that the BH mass can be as low as $10^5\,M_\odot$). For example, if the two flares are a result of multiple accretion-driven outflows, or discrete ejections of dense blobs of material (also referred to as a "knot ejection"; see, e.g., A. L. King et al. 2016), it is unclear why multiple outflows are not observed in all TDEs, and can be a result of the different mass scaling if AT 2024tvd is an IMBH TDE. Furthermore, if the double-peaked radio light curve is a result of a complex density profile, it can be related to the origin of this off-nuclear MBH (i.e., a recoiling MBH or an MBH from a minor galaxy merger) and the stellar population around it. On the other hand, it is important to note that there is a wide range of radio properties observed for different TDEs. Therefore, it is possible that this unique behavior is just another layer of an already complex landscape of TDEs in the radio. In the following discussion, we explore several astrophysical scenarios for the radio emission from AT 2024tvd in an attempt to explain the origin of both radio flares with a single outflow.

T. Matsumoto & T. Piran (2024) suggested that double-peaked radio light curves can result from the flattening of the density profile at the Bondi radius. Interestingly, in our equipartition analysis we find that the outflow radius at the time of the second radio flare is $\sim 6 \times 10^{16}$ cm, similar to the Bondi radius inferred by T. Matsumoto & T. Piran (2024) for a $10^6\,M_\odot$ BH and an ISM temperature of 10^7 K. However, this temperature is higher than expected for a warm ISM. On the other hand, as the environment of a non-AGN MBH is determined by the mass and energy injection from the surrounding stellar population (E. Quataert 2004; A. Generozov et al. 2015), a density break is also expected at the stagnation radius, R_s, that separates the inflow to the MBH from the outward stellar winds (A. Generozov et al. 2015; A. Yalinewich et al. 2018):

$$R_s \simeq 2.5\frac{GM_{\rm BH}}{v_w^2} \simeq 3 \times 10^{16}\,{\rm cm}\left(\frac{M_{\rm BH}}{10^6\,M_\odot}\right)\left(\frac{v_w}{1000\,{\rm km\,s^{-1}}}\right)^{-2}, \quad (10)$$

where $M_{\rm BH}$ is the mass of the BH and v_w is related to the heating of the gas by stellar winds. Based on the normalization of Equation (10) and the density we infer at $\approx R_s$, a high pre-TDE accretion rate is expected for a $10^6\,M_\odot$ BH:

$$\dot{M} \simeq 4\pi R_s^2 m_p n_e(R_s) v_{\rm ff} \simeq 0.03\dot{M}_{\rm Edd}\left(\frac{n_e(R_s)}{4 \times 10^4\,{\rm cm^{-3}}}\right)\left(\frac{R_s}{3 \times 10^{16}\,{\rm cm}}\right)^{3/2} \times \left(\frac{M_{\rm BH}}{10^6\,M_\odot}\right)^{-1/2}, \quad (11)$$

where the freefall velocity $v_{\rm ff} \equiv \left(\frac{GM_{\rm BH}}{R_s}\right)^{1/2}$ is estimated at the stagnation radius. Therefore, if the double-peaked radio light curve is a result of a break in the density profile at the stagnation radius, high accretion rate and wind velocities are needed. This implies a very young stellar population of $\tau_* \sim 10^7$ yr around this off-nuclear MBH (A. Generozov et al. 2015). Equation (10) is scaled to achieve a stagnation radius roughly at the same radius that we infer for the density break for $M_{\rm BH} \gtrsim 10^6\,M_\odot$. In order to achieve the same radius in the IMBH scenario, lower wind velocities are required, which result in an older stellar population. While the presence of the stagnation radius explains the observed break in the density profile, the slopes of the inferred density profiles, especially at $r < R_s$, are relatively steep and are not easily explained in this scenario.

A different natural explanation for the break in the density profile is that the radio-emitting shock first interacts with either the stellar debris or an early launched spherical outflow and only later interacts with the CNM. Since these early outflows are expected to travel at a velocity of a few $\times 10^4\,{\rm km\,s^{-1}}$, if they are launched around the time of optical discovery, they can reach a radius of a few $\times 10^{16}$ cm at the time of first radio detection ($\Delta t = 131$ days). Therefore, it is possible that an accretion-driven outflow that was launched at $\Delta t \approx 80$ days after optical discovery is first catching up with this early outflow, producing the first radio flare, and that the late rebrightening is due to the transition of the outflow to the CNM. This scenario can potentially explain the two distinct density structures and the steep density profile as being measured at the edge of an early spherical outflow or of the stellar debris. On the other hand, our analysis assumes a spherical outflow and that the geometry of the stellar debris in this scenario is inconsistent with the radii we infer. That is, the stellar debris stream is expected to be gravitationally bound and stretch only a few tens of solar radii in diameter (E. R. Coughlin et al. 2016). For a gravitationally bound stellar stream stretching a few $\times 10^{16}$ cm and with a width of

$\sim 10^{12}$ cm, the radio-emitting region appears smaller than it appears for a spherical interaction region and has an area filling factor of $f_A \sim 10^{-4}$. The radius of the emitting region scales as $f_A^{-8/19}$ (J. Krolik et al. 2016). Therefore, the radii we infer in the case of an interaction with a gravitationally bound stream are larger by more than an order of magnitude than for a spherical outflow and are not consistent with a subrelativistic tidal debris stream. We also emphasize that while the equipartition radius and the double-peaked radio light curve motivate a broken power-law density profile around the MBH, we cannot explain the accelerating shock during the second radio flare.

The discussion above is focused on a subrelativistic outflow. However, a double-peaked radio light curve is also expected, in some cases, for relativistic jets observed off-axis. For example, a double-peaked nonthermal emission component is sometimes discussed in GRBs for some viewing angles if the jet is structured (P. Beniamini et al. 2020), or when the reverse shock crosses the ejecta as it decelerates, resulting in two emission zones peaking at different times (E. Abdikamalov & P. Beniamini 2025). However, in the case of AT 2024tvd, even if we set the jet launch day to $t_{\rm launch} \approx 80$ days, the temporal evolution of the optically thin emission during the rebrightening is $F_\nu \sim t^{-8}$, which is too fast even for an off-axis jet (see Figure 6). O. Teboul & B. D. Metzger (2023) presented another scenario in which some relativistic jets launched by TDEs can only be observed at late times (see also W. Lu et al. 2024). In cases of misalignment between the spin of the MBH and the orbital plane of the disrupted star, the disk/jet structure will precess and a large quasi-spherical structure might be formed. The jet can then escape prior to, or at, the alignment with the spin of the MBH, depending on the alignment mechanism, i.e., magneto-spin versus hydrodynamic. Based on the observed timescales for AT 2024tvd and for an MBH with $10^6\,M_\odot$, hydrodynamic alignment of the disk/jet system, due to internal stresses within the accretion disk, is more likely. Furthermore, O. Teboul & B. D. Metzger (2023) find that for such a BH mass and for a disk viscosity parameter $\alpha \simeq 0.1$ the alignment timescale is $\sim$193 days, similar to our first detection of the second radio component. Therefore, we consider it plausible that both radio flares are a result of the same jet entering our line of sight as it precesses and that the onset of the second radio flare is at the alignment of the orbital plane with the MBH spin. However, in that case, the jet needs to align directly into our line of sight, or significantly decelerate and expand to a quasi-spherical outflow. This is somewhat supported by the high velocities we infer during the second radio flare even in the Newtonian regime. Further modeling is needed to determine the likelihood of this scenario.

6. Summary and Conclusions

This work presents the radio emission from the first optically selected off-nuclear TDE, AT 2024tvd. Our extensive radio campaign results in broadband observations in the range of 1.5–230 GHz, spanning from 88 days to $\sim$10 months after optical discovery, making AT 2024tvd one of the best-studied TDEs in radio wavelengths so far. In addition to its nontraditional position $\sim$0.8 kpc from the host nucleus, the temporal evolution of the radio emission from this TDE is unprecedented. Its double-peaked radio light curve is evolving faster than any other known TDE, with $F_\nu \sim t^{-6}$ and $\sim t^{-12}$ during the first and second radio components, respectively. In addition, the broadband SEDs revealed changes in the spectral slope of the optically thin regime and a monotonically declining radio spectral peak during the first radio component. However, a fast optically thin decline and an increasing radio spectral peak are observed during the second radio component.

Our analysis focuses on the nature of the radio-emitting outflow/outflows, i.e., relativistic versus nonrelativistic, and their launch time (promptly after optical discovery vs. delayed outflow). The overall emission is consistent with nonrelativistic, mildly relativistic, and/or ultrarelativistic outflows. However, based on the temporal indices, it is unlikely that an outflow that was launched at, or around, the time of optical discovery is responsible for any of the radio components, and there is strong evidence for delayed outflow(s). The first radio component is consistent with an outflow that is launched at $t_{\rm launch} \approx 80$ days, which coincides with the emergence of a Comptonized spectral component in the X-rays, possibly hinting toward an accretion-driven outflow.

The second flare is consistent with either a mildly relativistic ($\sim 0.5c$) outflow launched at $t_{\rm launch} \approx 170$ days or a relativistic jet (up to $\Gamma \sim 12$ for $\theta = 30^\circ$, launched at $t_{\rm launch} \approx 190$ days, only $\sim$4 days before the first detection of the second radio component). On the other hand, we note that we cannot rule out a scenario in which both flares are from the same subrelativistic outflow that was launched at $t_{\rm launch} \approx 80$ days. In this case the double-peaked radio light curve is a manifestation of a shock wave interacting with a broken power-law density profile. We show that such a density break is expected around the stagnation radius. We also raise the possibility that either the stellar debris or an early launched spherical outflow is the medium with which the delayed outflow first interacts before reaching the more distant CNM, resulting in the apparent transition in the density profile.

It is also worth highlighting that AT 2024tvd is the first radio-bright, bona fide off-nuclear TDE, and it is also the TDE with the fastest evolution observed to date. We therefore put forward the idea of a connection between the unique radio emission and the off-nuclear (and possibly intermediate-mass) origin of the MBH. On the other hand, it is also relevant to point out that the evolution of the thermal emission from this TDE observed in optical–UV–X-ray wavelengths is rather standard for a TDE (Y. Yao et al. 2025b). Furthermore, radio emission from TDEs does not seem to follow a well-defined evolution, and the emission has been observed to evolve quickly and peak on different timescales for different TDEs. Therefore, it is also possible that the unique evolution of the radio emission and the off-nuclear position are not related.

In order to break some of the model degeneracies and determine whether the radio-emitting outflows are relativistic or nonrelativistic, high-resolution, very long baseline interferometry observations are required to resolve a jet structure and/or detect the movement of a relativistic jet. Polarization measurements at different times can also help differentiate between subrelativistic and relativistic outflows since the emission is expected to be more polarized around the time of the peak of a jetted outflow (R. Gill & J. Granot 2018). In addition, early observations in the millimeter bands are sometimes the only way to constrain the outflow launch date, as an absorbed emission is expected to first peak in those bands. We plan to continue monitoring the radio emission from AT 2024tvd in an attempt to better understand the nature of this event.

Acknowledgments

We thank the anonymous referee for providing helpful comments that helped improve this work.

The National Radio Astronomy Observatory (NRAO) is a facility of the National Science Foundation operated under cooperative agreement by Associated Universities, Inc. We thank the NRAO for carrying out the Karl G. Jansky Very Large Array (VLA) and the Atacama Large Millimeter Array (ALMA) observations. This Letter makes use of the following ALMA data: ADS/JAO.ALMA#2024.A.00024.T, and ADS/JAO.ALMA#2024.A.00034.T. ALMA is a partnership of ESO (representing its member states), NSF (USA) and NINS (Japan), together with NRC (Canada), MOST and ASIAA (Taiwan), and KASI (Republic of Korea), in cooperation with the Republic of Chile. The Joint ALMA Observatory is operated by ESO, AUI/NRAO and NAOJ. The Allen Telescope Array refurbishment program and its ongoing operations are being substantially funded through the Franklin Antonio Bequest. Additional contributions from Frank Levinson, Greg Papadopoulos, the Breakthrough Listen Initiative, and other private donors have been instrumental in the renewal of the ATA. Breakthrough Listen is managed by the Breakthrough Initiatives, sponsored by the Breakthrough Prize Foundation. The Paul G. Allen Family Foundation provided major support for the design and construction of the ATA, alongside contributions from Nathan Myhrvold, Xilinx Corporation, Sun Microsystems, and other private donors. The ATA has also been supported by contributions from the US Naval Observatory and the US National Science Foundation. We acknowledge the staff who operate and run the AMI-LA telescope at Lord's Bridge, Cambridge, for the AMI-LA radio data. AMI is supported by the Universities of Cambridge and Oxford and by the European Research Council under grant ERC-2012-StG-307215 LODESTONE. The Submillimeter Array is a joint project between the Smithsonian Astrophysical Observatory and the Academia Sinica Institute of Astronomy and Astrophysics and is funded by the Smithsonian Institution and the Academia Sinica. We recognize that Maunakea is a culturally important site for the indigenous Hawaiian people; we are privileged to study the cosmos from its summit.

R.M. acknowledges partial support from the National Science Foundation (grant No. AST-2224255). K.D.A. and C.T.C. acknowledge support provided by the NSF through award SOSPA9-007 from the NRAO and award AST-2307668. K.D.A. gratefully acknowledges support from the Alfred P. Sloan Foundation. B.D.M. acknowledges partial support from the National Science Foundation (grant No. AST-2406637) and the Simons Foundation (grant No. 727700). The Flatiron Institute is supported by the Simons Foundation. P.B. was supported by a grant (No. 2020747) from the United States–Israel Binational Science Foundation (BSF), Jerusalem, Israel (PB), and by a grant (No. 1649/23) from the Israel Science Foundation. A.J.G. is grateful for support from the Forrest Research Foundation. N.F. acknowledges support from the National Science Foundation Graduate Research Fellowship Program under grant No. DGE-2137419. R.B.D. acknowledges support from the National Science Foundation under grant 2107932. This work was supported by the Australian government through the Australian Research Council's Discovery Projects funding scheme (DP200102471).

Software: astropy (Astropy Collaboration et al. 2013, 2018), `emcee` (D. Foreman-Mackey et al. 2013), CASA (CASA Team et al. 2022).

Appendix A
Prompt Subrelativistic Outflow Fit

In Section 4.2 we considered a delayed, subrelativistic outflow as the origin of the first flare. We showed that our multiepoch fit for such an outflow explains all the observed properties of the first flare. We also noted that the same fitting procedure requires extreme outflow parameters under the assumption of a prompt subrelativistic outflow. Here we briefly present the results of the prompt outflow fitting process, discuss its implications, and conclude that it is disfavored.

We consider the same model discussed in Section 4.2, but we introduce three main changes: (i) we adopt $t_{\rm launch} = 0$ days; (ii) ϵ_e is a free parameter, which is now possible since this model requires high densities to explain the first upper limit and we are provided with a measurement of the mass in front of the shock by the FFA, and therefore ϵ_e and ϵ_B are no longer degenerate; and (iii) we define $\nu_c = \min[\nu_{\rm sync}, \nu_{\rm IC}]$. To calculate $\nu_{\rm IC}$, we use the IC cooling Lorentz factor (e.g., A. J. Nayana et al. 2025)

$$\gamma_{\rm IC} = \frac{3\pi m_e c^2 r^2}{\sigma_{\rm T}\Gamma(\Delta t - t_{\rm launch})L_{\rm bol}} \approx 1.16 \times 10^{19}\frac{r^2}{\Gamma(\Delta t - t_{\rm launch})L_{\rm bol}}, \quad \text{(A1)}$$

where r is the radius of the radio-emitting shock, Γ is the bulk Lorentz factor, and we use the thermal optical/UV luminosity during the time of the first radio flare $L_{\rm bol} = 4.5 \times 10^{43}\left(\frac{\Delta t}{68\ \rm days}\right)^{-1.6}$ erg s^{-1} (Y. Yao et al. 2025, in preparation). We do not consider here the uncertainty on $L_{\rm bol}$, but we note that it has negligible impact on our conclusions.

We present in Figure 9 the evolution of the break frequencies, the inferred energy, and the density profiles of our delayed and prompt nonrelativistic outflow models. We find that while there is a set of parameters that provide a statistically acceptable fit to the observed broadband radio emission (including the early upper limit), the inferred values are physically extreme. For example, the post-shock energy is a few $\times 10^{52}$ erg, significantly higher than the energy we infer for any other scenario and for other radio-bright TDEs with subrelativistic outflows. Furthermore, the density profile is extremely steep, $n_e \sim r^{-6}$, and implies higher densities at $R \lesssim 10^{17}$ cm than any other radio-bright TDE. Based on this analysis, we conclude that the origin of the first flare is unlikely to be related to a prompt, nonrelativistic outflow.

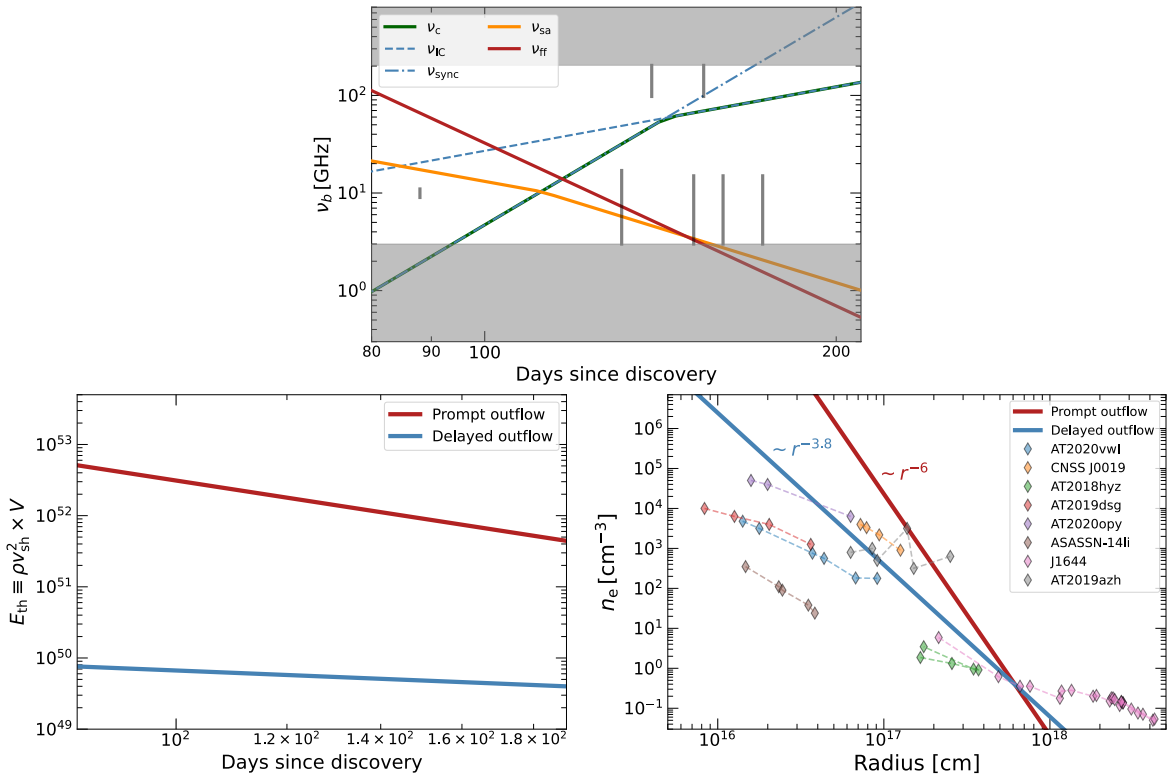

Figure 9. Results from our time-dependent fit of the first radio flare assuming a prompt nonrelativistic outflow. The top panel is for the temporal evolution of the different break frequencies based on our best-fitting parameters: $\beta_0 = 0.14 \pm 0.02$, $\log(n_0\,[\mathrm{cm}^{-3}]) = 7.36 \pm 0.07$, $k = 6.05 \pm 0.25$, $p = 2.05 \pm 0.05$, $\log(\epsilon_e) = -4.6 \pm 0.5$, and $\log(\epsilon_B) = -3.5 \pm 0.2$. The bottom left panel shows the post-shock energy for both the prompt and delayed outflows. Finally, the bottom right panel presents the density profiles we infer in each scenario compared to other radio-bright TDEs. Both the energetics and densities inferred in the prompt outflow scenario are extreme when compared to the other scenarios we explored in this work and other radio-bright TDEs.

Appendix B
Emission from the Host Galaxy Nucleus

As mentioned in Section 2, some of our observations showed two point sources: one at the known optical position of the TDE AT 2024tvd, and the other at the optical position of the center of the host galaxy (see coordinates reported in Y. Yao et al. 2025b). We construct an SED of the host galaxy nucleus by taking flux measurements at two different epochs from VLA observations taken in A configuration: $\Delta t = 88$ days for the X-band image, and $\Delta t = 160$ days for the S, C, and Ku bands (Figure 10). The emission is optically thin, and we find a best-fitting $F_\nu = A\left(\frac{\nu}{5\,\mathrm{GHz}}\right)^{-\beta}$ with $A = 64 \pm 4\,\mu$Jy and $\beta = 0.53 \pm 0.12$. Based on this fit, we estimate $L_{1.4\,\mathrm{GHz}} = (3.2 \pm 0.5) \times 10^{37}\,\mathrm{erg\,s^{-1}\,Hz^{-1}}$. Adopting the relation between the star formation rate (SFR) and the 1.4 GHz luminosity from L. J. M. Davies et al. (2017), we infer an SFR of $0.51 \pm 0.06\,M_\odot\,\mathrm{yr}^{-1}$. This value is significantly higher than the SFR constraints, $\leqslant 0.1\,M_\odot\,\mathrm{yr}^{-1}$, derived from stellar population synthesis analysis (C. Maraston et al. 2009). Therefore, as concluded by Y. Yao et al. (2025b), the radio source at the center of the galaxy must be powered by a low-luminosity AGN with a steep radio spectrum, possibly associated with a jet (A. Merloni et al. 2003).

We use this host galaxy radio model to estimate the contamination component for the observations obtained with the VLA when it was in C and D configurations and subtract it from the TDE emission (in S, C, and X bands). However, we note that this is a minor correction of less than 10% of the flux measurements for these observations.

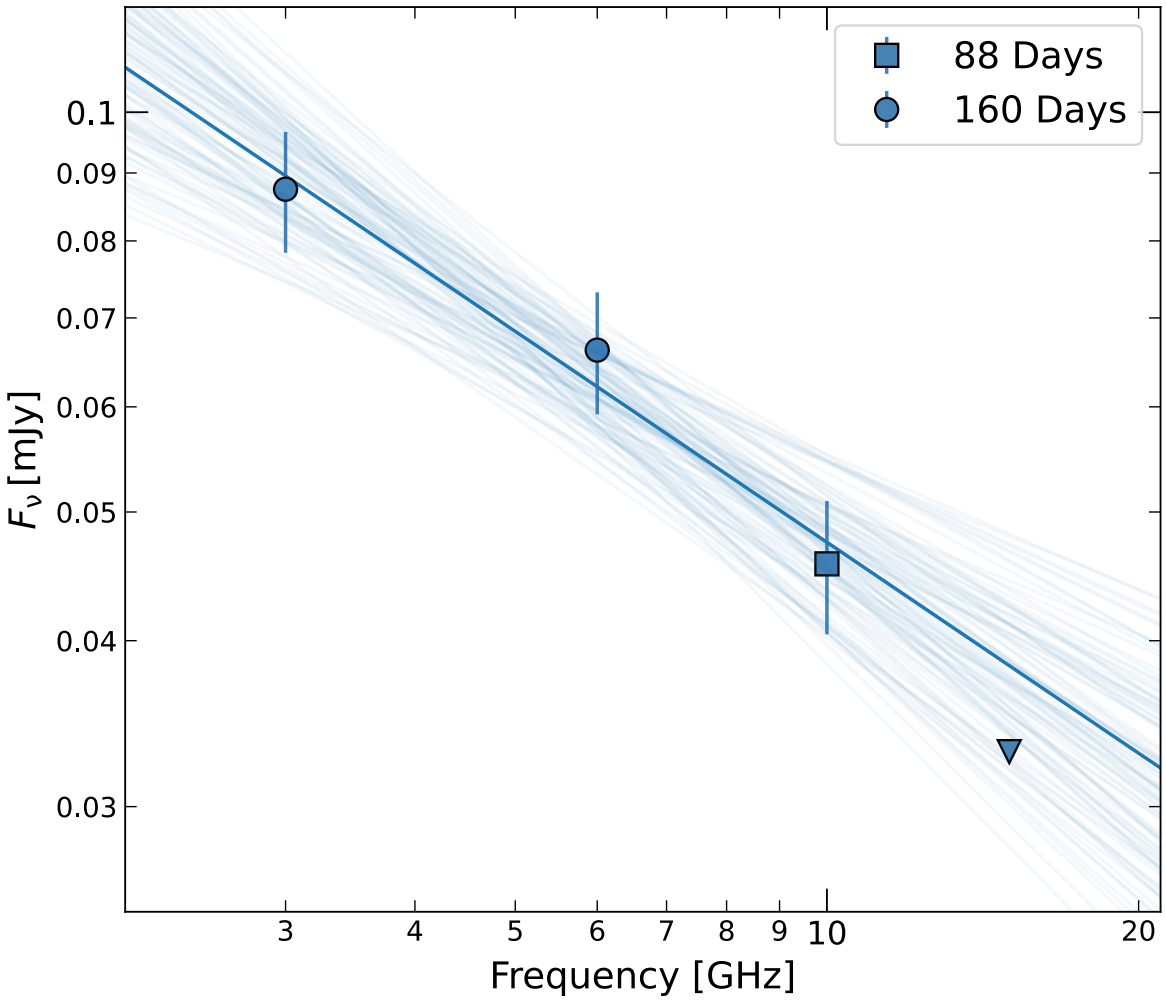

Figure 10. Broadband SED of the emission from the host galaxy nucleus. The filled circles are for radio detections obtained at $\Delta t = 160$ days, the square is for the detection obtained at $\Delta t = 88$ days, and the triangle is a 3σ upper limit obtained at $\Delta t = 160$ days. Also plotted is the best-fitting power-law (solid line) and models drawn from the posterior distribution.

Appendix C
Synchrotron Self-absorption Frequency in the Slow-cooling Regime

The synchrotron emission from astrophysical transients has been studied extensively, and multiple frameworks have been developed to infer the physical parameters from observed radio SEDs (e.g., R. A. Chevalier 1998; R. Sari et al. 1998; J. Granot & R. Sari 2002; R. Barniol Duran et al. 2013; L. Sironi & D. Giannios 2013; B. Margalit & E. Quataert 2021; T. Matsumoto & T. Piran 2021, 2023). Sometimes assumptions from nonequipartition frameworks have been combined in the TDE literature, leading to results that are not self-consistent. Thus motivated, in the next section we derive all the synchrotron break frequencies for different orderings of ν_m, $\nu_{\rm sa}$, ν_c in the slow-cooling regime ($\nu_{\rm m} < \nu_{\rm c}$; R. Sari et al. 1998), for a nonrelativistic outflow, and provide a recipe for calculating synchrotron SEDs (we provide the code used to calculate the synchrotron SEDs based on this method at https://github.com/Itaisfa/full_synchrotron_SED/tree/main; see also I. Sfaradi 2025).

Consider a shock moving with a bulk Lorentz factor Γ and a velocity $v_{\rm sh}$ and located at a redshift z and a luminosity distance d_l. At the shock front electrons are accelerated to a power-law energy distribution of the form

$$N(\gamma)d\gamma = N_0(\gamma/\gamma_m)^{-p}d\gamma;\ \ \gamma > \gamma_m, \tag{C1}$$

with

$$\gamma_m = \max\left[1, 4\epsilon_e\frac{p-2}{p-1}\frac{m_p}{m_e}\left(\frac{v_{\rm sh}}{c}\right)^2\right], \tag{C2}$$

where the factor of 4 arises from the definition of ϵ_e as a fraction of post-shock energy that goes to the relativistic electrons and the Rankine–Hugoniot jump conditions; m_e and m_p are the electron and proton masses, respectively. T. Matsumoto & T. Piran (2021) considered a minimum Lorentz factor of 2. Here we used a minimum $\gamma_m = 1$ for self-consistency with R. A. Chevalier (1998). We also find, for $p > 2$, that $N_0 \equiv N(\gamma = \gamma_m)$ is

$$N_0 = \frac{\epsilon_e}{\epsilon_B}\frac{B^2(p-2)}{8\pi\gamma_m^2 m_e c^2} \tag{C3}$$

by calculating $E_e = \int_{\gamma_m}^{\infty} N_0(\gamma/\gamma_m)^{-p}(\gamma m_e c^2)d\gamma$ and requiring $\frac{E_e}{\epsilon_e} = \frac{E_B}{\epsilon_B}$. Note that this analysis is compatible with the deep

Newtonian limit (L. Sironi & D. Giannios 2013) and that by setting the energy in the magnetic fields to be a fraction of the post-shock energy we reproduce the number of emitting electrons in the deep Newtonian limit (T. Matsumoto & T. Piran 2021). We also note that implementing this model with a lower limit of $\gamma_m = 2$ (instead of 1) results in a higher ratio of ϵ_e/ϵ_B.

The critical Lorentz factor below which the electron does not lose a significant fraction of its energy to radiation (i.e., the synchrotron cooling Lorentz factor) is

$$\gamma_c = \frac{6\pi m_e c}{\sigma_{\rm T}\Gamma B^2 t}, \tag{C4}$$

where B is the magnetic field strength, $\sigma_{\rm T}$ is the Thomson cross section, and c is the speed of light. The relativistic correction using the bulk Lorentz factor, Γ, is presented here for completeness, but we note that our analysis is always in the subrelativistic regime (i.e., for any practical purpose $\Gamma = 1$). The characteristic synchrotron frequency of an electron with Lorentz factor γ is

$$\nu(\gamma) = \frac{q_e B\Gamma\gamma^2}{2\pi m_e c(1+z)}, \tag{C5}$$

where q_e is the electric charge. Now we can derive the minimal and cooling frequencies, ν_m and ν_c, by replacing γ_m and γ_c, respectively, with γ in Equation (C5).

Following R. Sari et al. (1998), the flux density at the peak of the synchrotron emission is[35]

$$\begin{aligned} F_{\nu,\,\rm max} &\equiv P_{\nu,\,\rm max} N_{e,\rm iso}\frac{1}{4\pi d_l^2}(1+z) \\ &= \frac{m_e c^2\sigma_{\rm T}}{3q_e}\Gamma B N_{e,\rm iso}\frac{1}{4\pi d_l^2}(1+z), \end{aligned} \tag{C6}$$

where q_e is its electric charge, c is the speed of light, and $N_{e,\rm iso}$ is the isotropic equivalent number of emitting electrons. We assume that the number of emitting electrons at $\gamma_{\rm m}$ can be parameterized as

$$N_{e,\rm iso} = N_0 \times \frac{4\pi}{3} f R^3, \tag{C7}$$

where $\frac{4\pi}{3}fR^3$ is the emitting volume and f is the volume filling factor.

For different ordering of ν_m, $\nu_{\rm sa}$, ν_c, the flux density at $\nu_{\rm sa}$, $F_{\nu_{\rm sa}}$, will be a different function of these frequencies, $F_{\nu,\,\rm max}$, and p (based on the different spectral shapes discussed in J. Granot & R. Sari 2002):

$$F_{\nu_{\rm sa}} = \begin{cases} F_{\nu,\,\rm max}\left(\frac{\nu_{\rm sa}}{\nu_m}\right)^{1/3} & \nu_{\rm sa} < \nu_m < \nu_c \\ F_{\nu,\,\rm max}\left(\frac{\nu_{\rm sa}}{\nu_m}\right)^{-(p-1)/2} & \nu_m < \nu_{\rm sa} < \nu_c \\ F_{\nu,\,\rm max}\left(\frac{\nu_c}{\nu_m}\right)^{-(p-1)/2}\left(\frac{\nu_{\rm sa}}{\nu_c}\right)^{-p/2} & \nu_m,\,\nu_c < \nu_{\rm sa} \end{cases}. \tag{C8}$$

Now we can derive the SSA frequency by requiring that the flux at $\nu_{\rm sa}$ (defined in Equation (C8)) is equal to the blackbody flux given by

$$F_{\nu,\,\rm BB} = \frac{2\nu^2}{c^2}k_{\rm B}T f_A\frac{R^2}{d_l^2}\Gamma(1+z)^3, \tag{C9}$$

where $k_{\rm B}$ is Boltzmann's constant, T is the blackbody temperature, f_A is the area filling factor, and considering that at the low end of the energy distribution $k_{\rm B}T = \gamma m_e c^2$. This procedure gives

$$\nu_{\rm sa} = \begin{cases} \left[\bar{A}\frac{N_{e,\rm iso}B}{\gamma_m f_A R^2(1+z)^2\nu_m^{1/3}}\right]^{3/5} & \nu_{\rm sa} < \nu_m < \nu_c \\ \left[\bar{A}\bar{B}\frac{N_{e,\rm iso}B^{3/2}\Gamma^{1/2}}{f_A R^2(1+z)^{5/2}\nu_m^{-(p-1)/2}}\right]^{2/(p+4)} & \nu_m < \nu_{\rm sa} < \nu_c, \\ \left[\bar{A}\bar{B}\frac{N_{e,\rm iso}B^{3/2}\Gamma^{1/2}}{f_A R^2(1+z)^{5/2}\nu_m^{-(p-1)/2}\nu_c^{-1/2}}\right]^{2/(p+5)} & \nu_m,\,\nu_c < \nu_{\rm sa} \end{cases} \tag{C10}$$

where, for convenience, we defined $\bar{A} \equiv \frac{\sigma_{\rm T}c^2}{24\pi q_e}$ and $\bar{B} \equiv \left(\frac{2\pi m_e c}{q_e}\right)^{-1/2}$. Finally, the observed peak of the SED (at the intersection between optically thin and thick regimes) is

$$F_p = \begin{cases} F_{\nu,\,\rm max}\ \text{at}\ \nu_p = \nu_m & \nu_{\rm sa} < \nu_m < \nu_c \\ F_{\nu,\,\rm max}\left(\frac{\nu_{\rm sa}}{\nu_m}\right)^{-(p-1)/2}\ \text{at}\ \nu_p = \nu_{\rm sa} & \nu_m < \nu_{\rm sa} < \nu_c \\ F_{\nu,\,\rm max}\left(\frac{\nu_c}{\nu_m}\right)^{-(p-1)/2}\left(\frac{\nu_{\rm sa}}{\nu_c}\right)^{-p/2}\ \text{at}\ \nu_p = \nu_{\rm sa} & \nu_m,\,\nu_c < \nu_{\rm sa} \end{cases}. \tag{C11}$$

Appendix D
Off-axis Equipartition Analysis for Electrons That Radiate at the Minimal Frequency

T. Matsumoto & T. Piran (2023) generalized the traditional equipartition analysis introduced in R. Barniol Duran et al. (2013) for a relativistic jetted emitter observed off-axis. However, their formalism, as mentioned in R. Barniol Duran et al. (2013), is only for electrons that radiate at a peak frequency ν_p. These electrons are likely to carry most of the relativistic electron energy only if $\nu_p = \nu_m$. However, if $\nu_m < \nu_{\rm sa}$, most of the energy is carried by electrons with the minimal Lorentz factor, γ_m, and the emission of which is self-absorbed, which means that we would be underestimating the energy without taking these electrons into account. We account for this additional energy by introducing a factor of $(\gamma_m/\gamma_e)^{2-p}$ to the energy of the electrons (as discussed in Section 4.2.1 in R. Barniol Duran et al. 2013), and we use it to

[35] As mentioned in R. Barniol Duran et al. (2013), the precise numerical prefactor depends on the power-law index of the energy distribution of the electrons p. We provide the numerical prefactor considered by taking the peak spectral power $P_{\nu,\,\rm max}$ and multiplying it by the number of emitting e^- at γ_m, $N_{e,\rm iso}$ (see R. Sari et al. 1998 and Equation (C7)). For a relativistic shock the number of emitting electrons in the emitting region is $N_e = N_{e,\rm iso}/4\Gamma^2$ (R. Barniol Duran et al. 2013).

generalize the process introduced in T. Matsumoto & T. Piran (2023) for any value of power-law index p.

Equations (8), (9), and (10) in T. Matsumoto & T. Piran (2023) give

$$\gamma_e = \frac{3F_p d_L^2 \eta^{\frac{5}{3}} \Gamma^2}{2\pi\nu_p^2 (1+z)^3 m_e f_A R^2 \delta_D} = 520 \left[\frac{F_{p,\mathrm{mJy}} d_{L,28}^2 \eta^{\frac{5}{3}}}{\nu_{p,10}^2 (1+z)^3}\right] \frac{\Gamma^2}{f_A R_{17}^2 \delta_D} \quad \text{(D1)}$$

$$N_e = \frac{9cF_p^3 d_L^6 \eta^{\frac{10}{3}} \Gamma^4}{2\sqrt{3}\,\pi^2 q_e^2 m_e^2 \nu_p^5 (1+z)^8 f_A^2 R^4 \delta_D^4} = 4.1 \times 10^{54} \left[\frac{F_{p,\mathrm{mJy}}^3 d_{L,28}^6 \eta^{\frac{10}{3}}}{\nu_{p,10}^5 (1+z)^8}\right] \frac{\Gamma^4}{f_A^2 R_{17}^4 \delta_D^4} \quad \text{(D2)}$$

$$B = \frac{8\pi^3 m_e^3 c \nu_p^5 (1+z)^7 f_A^2 R^4 \delta_D}{9 q_e F_p^2 d_L^4, \eta^{\frac{10}{3}} \Gamma^4} = 1.3 \times 10^{-2}\,\mathrm{G} \left[\frac{\nu_{p,10}^5 (1+z)^7}{F_{p,\mathrm{mJy}}^2 d_{L,28}^4 \eta^{\frac{10}{3}}}\right] \frac{f_A^2 R_{17}^4 \delta_D}{\Gamma^4}. \quad \text{(D3)}$$

The energy in the electrons is

$$E_e = N_e \gamma_e m_e c^2 \Gamma (\gamma_m/\gamma_e)^{2-p} = 3.36 \times 10^{48}\,\mathrm{erg} \times [520]^{p-1} \times F_{p,\mathrm{mJy}}^{p+2} d_{L,28}^{2(p+2)} \nu_p^{-(2p+3)} \times (1+z)^{-(3p+5)} \gamma_m^{2-p} f_A^{-(p+1)} \times R_{17}^{-(2p+2)} \Gamma^{2p+3} \delta_D^{-(p+3)}, \quad \text{(D4)}$$

and in the magnetic field

$$E_B = \frac{(B\Gamma)^2}{8\pi} V = 2.11 \times 10^{46}\,\mathrm{erg} \times F_{p,\mathrm{mJy}}^{-4} d_{L,28}^{-8} \nu_{p,10}^{10} (1+z)^{14} \times f_A^4 f_V R_{17}^{11} \Gamma^{-10} \delta_D^2. \quad \text{(D5)}$$

We next minimize the total energy with respect to the radius, and the energy is minimized at $E_B = \left(\frac{2p+2}{11}\right) E_e$. The equipartition radius is

$$R_{\mathrm{eq}} = (10^{17}\,\mathrm{cm})[159 \times [520]^{p-1}]^{\frac{1}{2p+13}} \times F_{p,\mathrm{mJy}}^{\frac{p+6}{2p+13}} d_{L,28}^{\frac{2(p+6)}{2p+13}} \nu_{p,10}^{-1} (1+z)^{-\frac{3p+19}{2p+13}} \times \epsilon^{\frac{1}{2p+13}} \gamma_m^{\frac{2-p}{2p+13}} f_A^{-\frac{p+5}{2p+13}} f_V^{-\frac{1}{2p+13}} \Gamma \delta_D^{-\frac{p+5}{2p+13}}, \quad \text{(D6)}$$

and the equipartition energy is

$$E_{\mathrm{eq}} = (3.36 \times 10^{48}\,\mathrm{erg})[159]^{-\frac{2(p+1)}{2p+13}} \times [520]^{\frac{11(p-1)}{2p+13}} F_{p,\mathrm{mJy}}^{\frac{3p+14}{2p+13}} d_{L,28}^{\frac{2(3p+14)}{2p+13}} \times \nu_{p,10}^{-1} (1+z)^{-\frac{5p+27}{2p+13}} \times \left[1 + \left(\frac{2p+2}{11}\right)\epsilon\right] \epsilon^{\frac{-2(p+1)}{2p+13}} \gamma_m^{\frac{11(2-p)}{2p+13}} \times f_A^{-\frac{3(p+1)}{2p+13}} f_V^{\frac{2(p+1)}{2p+13}} \Gamma \delta_D^{-\frac{7p+29}{2p+13}}. \quad \text{(D7)}$$

Here $\epsilon = \left(\frac{\epsilon_B}{\epsilon_e}\right)/\left(\frac{2p+2}{11}\right)$, and ϵ_e and ϵ_B are introduced to account for deviations from equipartition (similar to R. Barniol Duran et al. 2013). We also introduce factors of $\xi^{\frac{1}{2p+13}}$ and $\xi^{\frac{11}{2p+13}}$, with $\xi = 1 + \epsilon_e^{-1}$, to Equations (D6) and (D7), respectively, to account for hot protons (see discussion in Section 4.2.2 in R. Barniol Duran et al. 2013). Finally, it is important to note that, here, ϵ_B and ϵ_e are not defined as fraction of the post-shock energy and therefore are different from the definitions introduced for the nonrelativistic case (Appendix C and Equation (3)).

ORCID iDs

Itai Sfaradi https://orcid.org/0000-0003-0466-3779
Raffaella Margutti https://orcid.org/0000-0003-4768-7586
Ryan Chornock https://orcid.org/0000-0002-7706-5668
Kate D. Alexander https://orcid.org/0000-0002-8297-2473
Brian D. Metzger https://orcid.org/0000-0002-4670-7509
Paz Beniamini https://orcid.org/0000-0001-7833-1043
Rodolfo Barniol Duran https://orcid.org/0000-0002-5565-4824
Yuhan Yao https://orcid.org/0000-0001-6747-8509
Assaf Horesh https://orcid.org/0000-0002-5936-1156
Wael Farah https://orcid.org/0000-0002-0161-7243
Edo Berger https://orcid.org/0000-0002-9392-9681
Nayana A. J. https://orcid.org/0000-0002-8070-5400
Yvette Cendes https://orcid.org/0000-0001-7007-6295
Tarraneh Eftekhari https://orcid.org/0000-0003-0307-9984
Noah Franz https://orcid.org/0000-0003-4537-3575
Dave A. Green https://orcid.org/0000-0003-3189-9998
Erica Hammerstein https://orcid.org/0000-0002-5698-8703
Wenbin Lu https://orcid.org/0000-0002-1568-7461
Eli Wiston https://orcid.org/0009-0002-4843-2913
Joe Bright https://orcid.org/0000-0002-7735-5796
Collin T. Christy https://orcid.org/0000-0003-0528-202X
Luigi F. Cruz https://orcid.org/0000-0001-5576-2254
David R. DeBoer https://orcid.org/0000-0003-3197-2294
Walter W. Golay https://orcid.org/0000-0001-7946-1034
Adelle J. Goodwin https://orcid.org/0000-0003-3441-8299
Mark Gurwell https://orcid.org/0000-0003-0685-3621
Garrett K. Keating https://orcid.org/0000-0002-3490-146X
Tanmoy Laskar https://orcid.org/0000-0003-1792-2338
James C. A. Miller-Jones https://orcid.org/0000-0003-3124-2814
Alexander W. Pollak https://orcid.org/0000-0002-3430-7671
Ramprasad Rao https://orcid.org/0000-0002-1407-7944
Sofia Z. Sheikh https://orcid.org/0000-0001-7057-4999
Nadav Shoval https://orcid.org/0009-0005-5622-3611
Sjoert van Velzen https://orcid.org/0000-0002-3859-8074

References

Abdikamalov, E., & Beniamini, P. 2025, MNRAS, 539, 2707
Alexander, K. D., Berger, E., Guillochon, J., Zauderer, B. A., & Williams, P. K. G. 2016, ApJL, 819, L25
Alexander, K. D., Margutti, R., Gomez, S., et al. 2025, arXiv:2506.12729
Alexander, K. D., van Velzen, S., Horesh, A., & Zauderer, B. A. 2020, SSRv, 216, 81
Andreoni, I., Coughlin, M. W., Perley, D. A., et al. 2022, Natur, 612, 430
Astropy Collaboration, Price-Whelan, A. M., Sipőcz, B. M., et al. 2018, AJ, 156, 123

Astropy Collaboration, Robitaille, T. P., Tollerud, E. J., et al. 2013, A&A, 558, A33
Barniol Duran, R., Nakar, E., & Piran, T. 2013, ApJ, 772, 78
Bellm, E. C., Kulkarni, S. R., Barlow, T., et al. 2019, PASP, 131, 068003
Beniamini, P., Granot, J., & Gill, R. 2020, MNRAS, 493, 3521
Beniamini, P., Piran, T., & Matsumoto, T. 2023, MNRAS, 524, 1386
Berger, E., Zauderer, A., Pooley, G. G., et al. 2012, ApJ, 748, 36
Bonnerot, C., & Lu, W. 2020, MNRAS, 495, 1374
Bright, J. S., Rhodes, L., Farah, W., et al. 2023, NatAs, 7, 986
Butler, B. 2012, Atacama Large Millimeter/Submillimeter Array Memo, 594, 1
Caprioli, D. 2024, in Foundations of Cosmic Ray Astrophysics, ed. F. A. Aharonian et al. (Amsterdam: IOS Press), 143
CASA Team, Bean, B., Bhatnagar, S., et al. 2022, PASP, 134, 114501
Cendes, Y., Alexander, K. D., Berger, E., et al. 2021, ApJ, 919, 127
Cendes, Y., Berger, E., Alexander, K. D., et al. 2022, ApJ, 938, 28
Cendes, Y., Berger, E., Alexander, K. D., et al. 2024, ApJ, 971, 185
Cendes, Y., Berger, E., Beniamini, P., et al. 2025, arXiv:2507.08998
Chevalier, R. A. 1998, ApJ, 499, 810
Chevalier, R. A., & Fransson, C. 2006, ApJ, 651, 381
Christy, C. T., Alexander, K. D., Margutti, R., et al. 2024, ApJ, 974, 18
Coughlin, E. R., Nixon, C., Begelman, M. C., & Armitage, P. J. 2016, MNRAS, 459, 3089
Davies, L. J. M., Huynh, M. T., Hopkins, A. M., et al. 2017, MNRAS, 466, 2312
DeMarchi, L., Margutti, R., Dittman, J., et al. 2022, ApJ, 938, 84
Eftekhari, T., Berger, E., Zauderer, B. A., Margutti, R., & Alexander, K. D. 2018, ApJ, 854, 86
Faris, S., Arcavi, I., Newsome, M., et al. 2024, TNSCR, 2024-4005, 1
Fender, R. P., Belloni, T. M., & Gallo, E. 2004, MNRAS, 355, 1105
Foreman-Mackey, D., Conley, A., Meierjurgen Farr, W., et al., 2013 emcee: The MCMC Hammer, Astrophysics Source Code Library, ascl:1303.002
Generozov, A., Stone, N. C., & Metzger, B. D. 2015, MNRAS, 453, 775
Giannios, D., & Metzger, B. D. 2011, MNRAS, 416, 2102
Gill, R., & Granot, J. 2018, MNRAS, 478, 4128
Goodwin, A. J., Alexander, K. D., Miller-Jones, J. C. A., et al. 2023, MNRAS, 522, 5084
Goodwin, A. J., Burn, M., Anderson, G. E., et al. 2025a, ApJS, 278, 36
Goodwin, A. J., Mummery, A., Laskar, T., et al. 2025b, ApJ, 981, 122
Goodwin, A. J., van Velzen, S., Miller-Jones, J. C. A., et al. 2022, MNRAS, 511, 5328
Graham, M. J., Kulkarni, S. R., Bellm, E. C., et al. 2019, PASP, 131, 078001
Granot, J., & Sari, R. 2002, ApJ, 568, 820
Grotova, I., Rau, A., Baldini, P., et al. 2025, A&A, 697, A159
Guolo, M., Gezari, S., Yao, Y., et al. 2024, ApJ, 966, 160
Guolo, M., & Mummery, A. 2025, ApJ, 978, 167
Hajela, A., Alexander, K. D., Margutti, R., et al. 2025, ApJ, 983, 29
Hammerstein, E., van Velzen, S., Gezari, S., et al. 2023, ApJ, 942, 9
Hickish, J., Razavi-Ghods, N., Perrott, Y. C., et al. 2018, MNRAS, 475, 5677
Hills, J. G. 1975, Natur, 254, 295
Högbom, J. A. 1974, A&AS, 15, 417
Horesh, A., Bernstein, Y., Bright, J., et al. 2025, TNSAN, 20, 1
Horesh, A., Cenko, S. B., & Arcavi, I. 2021a, NatAs, 5, 491
Horesh, A., Sfaradi, I., Fender, R., et al. 2021b, ApJL, 920, L5
Jin, C. C., Li, D. Y., Jiang, N., et al. 2025, arXiv:2501.09580
King, A. L., Miller, J. M., Bietenholz, M., et al. 2016, NatPh, 12, 772
Krolik, J., Piran, T., Svirski, G., & Cheng, R. M. 2016, ApJ, 827, 127
Lin, D., Strader, J., Carrasco, E. R., et al. 2018, NatAs, 2, 656
Lin, D., Strader, J., Romanowsky, A. J., et al. 2020, ApJL, 892, L25
Lu, W., Matsumoto, T., & Matzner, C. D. 2024, MNRAS, 533, 979
Maraston, C., Strömbäck, G., Thomas, D., Wake, D. A., & Nichol, R. C. 2009, MNRAS, 394, L107
Margalit, B., & Quataert, E. 2021, ApJL, 923, L14
Margutti, R., Soderberg, A. M., Chomiuk, L., et al. 2012, ApJ, 751, 134
Matsumoto, T., & Piran, T. 2021, MNRAS, 507, 4196
Matsumoto, T., & Piran, T. 2023, MNRAS, 522, 4565
Matsumoto, T., & Piran, T. 2024, ApJ, 971, 49
Merloni, A., Heinz, S., & di Matteo, T. 2003, MNRAS, 345, 1057
Mimica, P., Giannios, D., Metzger, B. D., & Aloy, M. A. 2015, MNRAS, 450, 2824
Nayana, A. J., Margutti, R., Wiston, E., et al. 2025, ApJ, 985, 51
Pacholczyk, A. G. 1970, Radio Astrophysics. Nonthermal Processes in Galactic and Extragalactic Sources, Series of Books in Astronomy and Astrophysics (San Francisco, CA: Freeman)
Perrott, Y. C., Scaife, A. M. M., Green, D. A., et al. 2013, MNRAS, 429, 3330
Piro, A. L., & Mockler, B. 2025, ApJ, 985, 77
Quataert, E. 2004, ApJ, 613, 322
Rees, M. J. 1988, Natur, 333, 523
Rhodes, L., Bright, J. S., Fender, R., et al. 2023, MNRAS, 521, 389
Ricarte, A., Tremmel, M., Natarajan, P., & Quinn, T. 2021a, ApJL, 916, L18
Ricarte, A., Tremmel, M., Natarajan, P., Zimmer, C., & Quinn, T. 2021b, MNRAS, 503, 6098
Rybicki, G. B., & Lightman, A. P. 1986, Radiative Processes in Astrophysics (New York: Wiley-VCH)
Sari, R., Piran, T., & Narayan, R. 1998, ApJL, 497, L17
Sfaradi, I. 2025, full_synchrotron_SED, v1, Zenodo, doi:10.5281/zenodo.17123238
Sfaradi, I., Beniamini, P., Horesh, A., et al. 2024, MNRAS, 527, 7672
Sfaradi, I., Chornock, R., Alexander, K. D., et al. 2025, TNSAN, 14, 1
Sfaradi, I., Horesh, A., Fender, R., et al. 2022, ApJ, 933, 176
Sironi, L., & Giannios, D. 2013, ApJ, 778, 107
Sollerman, J., Fremling, C., Perley, D., & Laz, T. D. 2024, TNSTR, 2024-3166, 1
Stein, R., van Velzen, S., Kowalski, M., et al. 2021, NatAs, 5, 510
Stone, N., & Loeb, A. 2011, MNRAS, 412, 75
Strubbe, L. E., & Quataert, E. 2009, MNRAS, 400, 2070
Teboul, O., & Metzger, B. D. 2023, ApJL, 957, L9
Titarchuk, L., & Seifina, E. 2021, MNRAS, 501, 5659
van Velzen, S., Gezari, S., Hammerstein, E., et al. 2021, ApJ, 908, 4
Waxman, E., & Shvarts, D. 1993, PhFlA, 5, 1035
Webb, N., Cseh, D., Lenc, E., et al. 2012, Sci, 337, 554
Weibel, E. S. 1959, PhRvL, 2, 83
Weiler, K. W., Sramek, R. A., Panagia, N., van der Hulst, J. M., & Salvati, M. 1986, ApJ, 301, 790
Yalinewich, A., Sari, R., Generozov, A., Stone, N. C., & Metzger, B. D. 2018, MNRAS, 479, 4778
Yao, Y., Chornock, R., Margutti, R., et al. 2025a, TNSAN, 13, 1
Yao, Y., Chornock, R., Ward, C., et al. 2025b, ApJL, 985, L48
Yao, Y., Ravi, V., Gezari, S., et al. 2023, ApJL, 955, L6
Zauderer, B. A., Berger, E., Soderberg, A. M., et al. 2011, Natur, 476, 425
Zwart, J. T. L., Barker, R. W., Biddulph, P., et al. 2008, MNRAS, 391, 1545